A STUDY OF DISK DRIVE DYNAMICS AT THE HEAD STACK ASSEMBLY LEVEL

Hany M. Gross and David B. Bogy
Computer Mechanics Laboratory
Department of Mechanical Engineering
University of California, Berkeley
Berkeley, CA 94720

Abstract

The demand for higher track density and lower flying height implies a corresponding decrease in the tolerances on the vibration levels in the drive, namely the allowable track misregistration and the allowable flying height modulation. On the other hand, the demand for higher disk rotational speeds implies stronger internally induced sources of vibration in the drive, primarily the windage excitation. With this decrease in the allowable vibration budgets and increase in the sources of excitation, effects that were formerly considered negligible are becoming quite significant. This motivates studying the dynamics of the disk drive at a higher level of complexity.

This report documents a study, using finite element analysis, which aimed at thoroughly investigating and understanding disk drive dynamics at the head stack assembly level. The approach adopted was to investigate the dynamic characteristics of the individual components of the head stack assembly, specifically the head gimbal assemblies and the actuator, and then investigate and understand the dynamic characteristics of the system as a whole in terms of the component dynamics and their coupling.

I. Introduction

The areal recording densities of hard disk drives (HDDs) have recently been increasing at an annual rate of 60%. The achievability of future industry goals for higher areal density is predicated upon attaining higher track densities and higher bit cell densities, the latter translating, at least in part, to lower flying heights. This, in turn, implies a corresponding decrease in the tolerances on the vibration levels in the drive. The allowable track misregistration (TMR) will decrease since the TMR must be kept to within 12% of the track width, and the allowable flying height modulation will also decrease. On the other hand, the demand for higher data throughput rates necessitates higher disk rotational speeds, which will result in stronger internally induced sources of vibration in the drive, primarily the windage excitation (or air turbulence excitation). In addition, the demand for lower access times translates into a demand for higher positioning speeds, and these would result in higher residual vibrations.

With this decrease in the allowable vibration budgets and increase in the sources of excitation, smaller variations in slider positioning pose a potential threat of read errors, write errors, or head slaps. Consequently, effects that were formerly considered negligible are becoming quite significant. This motivates studying the dynamics of the disk drive at a higher level of complexity.

Many studies have been dedicated to investigating the dynamics of the individual drive components, but very few have investigated ‘drive-level’ dynamics. Studies that focused

on individual components include [1] in which Yoshida et al. presented a new actuator design to reduce residual vibrations; [2] in which Ku investigated the dynamic characteristics of spindle motors and compared ball bearings with hydrodynamic bearings; [3] in which McAllister investigated the effect of platter resonances on TMR and found that axial disk vibration produces a significant portion of the TMR at 7,200 RPM; [4] in which Zeng and Bogy investigated the dynamic properties of a HGA using modal testing and finite element analysis.

Some of the studies carried out at the drive system level include [5] where Radwan and Whaley studied servo-structure interaction using finite element analysis and examined the effect of structural resonances on the open loop servo response of the drive; [6] where Wilson and Bogy carried out modal tests on suspensions loaded on spinning disks, and investigated the dynamic coupling of the suspension and disk modes; [7, 8] where Zeng and Bogy investigated the dynamic characteristics of hard disk drives using modal testing and finite element analysis.

The goal of this study is to thoroughly investigate and understand the dynamics of the hard disk drive at the head stack assembly (HSA) level. The approach adopted was to investigate the dynamic characteristics of the individual components of the HSA, namely the head gimbal assembly (HGA) and the actuator (the E-block/voice-coil unit), and then investigate and understand the dynamic behavior of the HSA as an integrated system in terms of the component dynamics and their coupling.

Finite element analysis was used in this study to understand the dynamic characteristics of the components and their coupling in the assembled system. The objective of the study was not to accurately identify the modal parameters of the HSA modeled, but rather to examine the dynamic behavior of the system and reach a better understanding and appreciation of the nature and complexity of its response. This is an essential prerequisite to accurate structural identification, modification, analysis, and design at the system level. Research plunging into such tasks without a keen understanding of the system response will likely be overwhelmed by the abundance of modes associated with such a complex structure.

II. Component and System Modeling

A better understanding of the system dynamics can be attained by first investigating and understanding the dynamics of its components. The main components of the HSA are the HGAs and the actuator. An HGA consists of the baseplate, the suspension load beam, the flexure, and the slider, and will be considered as a subsystem of the HSA without further subdivision. The actuator consists of the E-block with the actuator arms, and the voice coil, integrated together through the overmold encapsulation. All finite element modeling and analyses were carried out using ANSYS FE software. The HSA modeled was a two-platter HSA using Western Digital's "Rebel" E-block, and four Hutchinson conventional HTI 2030 suspensions. The details of the modeling and boundary conditions applied to each subsystem are described below.

II.I. The Head Gimbal Assemblies

A head gimbal assembly consists of the loadbeam, the flexure, the baseplate, and the slider. The loadbeam was modeled using 714 SHELL43 4-node structural shell elements with 872 nodes. The flexure was modeled using 130 SHELL43 4-node structural shell elements with 190 nodes, and was attached to the loadbeam at the laser spot weld locations using BEAM4 3-D elastic beam elements. The material properties used for both the loadbeam and the flexure were those of stainless steel and are listed in Table 1. The material used for the beam elements was assigned a high stiffness and low density so as to provide the desired attachment without affecting the dynamic properties of the system. The values used are listed in Table 1. The flexure dimple was also modeled using BEAM4 3-D elastic beam elements. The slider was modeled using MASS21 structural mass element, which is a single-node element that can be assigned a mass and rotational mass moments of inertia. It was given the following inertia properties which are typical of a pico slider:

$m = 1.71\times10^{-6}$ kg

$I_{xx} = I_{roll} = 0.141\times10^{-6}$ kg.mm^2

$I_{yy} = I_{pitch} = 0.221\times10^{-6}$ kg.mm^2

$I_{zz} = I_{yaw} = 0.343\times10^{-6}$ kg.mm^2

The slider mass element was positioned at the location of the center of gravity of the slider, and was attached to the flexure using BEAM4 3-D elastic beam elements (Fig. 3).

The baseplate was modeled using 1072 SOLID72 3-D 4-node tetrahedral structural solid elements with 406 nodes, and was attached to the loadbeam at the laser spot weld locations using BEAM4 3-D elastic beam elements.

The HGA was initially modeled as a flat structure (with a formed loadbeam and a formed flexure). It was then bent into the free state using a coordinate transformation of the appropriate nodes. Finally, to obtain the model for the HGA in the loaded state, a nonlinear static analysis[1] was performed in which the slider was loaded to the desired offset, and the coordinates of the nodes were updated to the deformed configuration (Figs. 1 and 2).

In the analyses of the HGA, the baseplate area of the loadbeam was completely constrained to have no degrees of freedom, so that its nodes can neither translate nor rotate in any direction. Since the baseplate would also be fully constrained in these analyses, it was removed from the model. Each HGA model contained 1,089 nodes. Ait bearing dynamics were not considered when performing the modal and harmonic analyses[2]; the slider was constrained to have a fixed flying attitude: fixed flying height (z translational DOF), fixed pitch (y rotational DOF), and fixed roll (x rotational DOF).

[1] A static analysis in ANSYS calculates the nodal displacements and element stresses due to applied loads (in the form of applied displacements of forces) at selected nodes.
[2] A modal analysis in ANSYS identifies the natural frequencies and mode shapes of the modeled structure. A harmonic analysis in ANSYS determines the response of the structure to sinusoidally varying loads (in the form of displacements or forces) applied at selected nodes.

II.II. The Actuator

The ANSYS auto-mesh was used to generate the FE mesh of the actuator (Figs. 14 and 15). The E-block, the voice coil, and the overmold encapsulation were modeled using 18,075 SOLID72 3-D 4-node tetrahedral structural solid elements with 5,156 nodes. Aluminum 6061-T6 material properties were used for the E-block, while aluminum material properties were used for the voice coil. These properties and the material properties used for the overmold encapsulation (which is usually made of fiber-reinforced polyethylene sulfide) are listed in Table 1.

The overmold arm supporting the flex cable exhibited a large number of modes in the modal analysis, none of which had any effect on the dynamics of the slider. This justified removing the flex cable arm from the model in order to reduce the size of the model and the size of the solution space. Many other details were included in the model that had very little effect on the dynamics of the system. These details were retained in this study, but are removed in a subsequent modified model which is to include more of the drive components.

The E-block pivot was modeled using BEAM4 3-D elastic beam elements attaching the nodes on the inner surface of the E-block overmold to a node at the center of the pivot core. This center node was constrained to have no translation, and was connected using a COMBIN14 torsional spring-damper element to a coincident node which was fixed in space. This was done to simulate the rigid body rotation mode of the E-block. The values

of the stiffness and damping (k = 500,000, c = 1,000) used for the spring damper element were concocted so that the natural frequency of the rigid body rotation mode is around 60 Hz [9].

II.III. The Head Stack Assembly

The HSA modeled was a two-platter HSA with four suspension assemblies. The four HGA's were connected to the E-block through common nodes at the area of the baseplate representing the swage area. The final HSA model (Figs. 24 and 25) consisted of 26,053 elements with 47,085 nodes.

III. Finite Element Analysis and Results

A modal analysis was carried out to obtain the modal parameters of each subsystem, and the associated mode shapes were examined. A harmonic analysis was then performed to obtain some frequency response functions (FRF) of each subsystem to a given excitation. The harmonic analyses focused mainly on FRFs associated with off-track vibrations. Descriptions of the excitations and parameters used in the modal and harmonic analyses are presented below.

The models of the E-block/voice-coil unit and the HGAs were then integrated to obtain a model of the HSA. Finite element modal and harmonic analyses of this model were carried out and the results were compared with those of the individual components. All analyses were performed over the frequency range 0-14 kHz.

III.I. The Head Gimbal Assembly

The natural frequencies and associated mode shapes of the HGA are listed in Table 2 and are shown in Figs. 4 through 12. HGA modes that contribute significantly to off-track motion include the three loadbeam torsion modes (T1, T2, T3), the sway mode (S), and mode 7 (FT1/T2) in which the flexure torsion couples with the loadbeam second torsion mode. HGA modes that contribute significantly to flying height modulation include the loadbeam bending modes (B1, B2, B3), and the flexure bending mode (FB) which couples weakly with the loadbeam third bending mode.

Fig. 13 shows an FRF of the HGA: the off-track response of the slider mass element to a unit lateral excitation at the baseplate area over the frequency range [0, 45] kHz. Note that the modes excited are those that contribute significantly to off-track vibration, and that the frequency range [0, 14] kHz contains only five such modes (those listed above).

III.II. The actuator

The natural frequencies and associated mode shapes of the actuator are listed in Table 3 and some of the mode shapes are shown in Figs. 16 through 24. The overmold section around the coil exhibits a large number of modes by virtue of its lower stiffness. However, the effect of these modes on the dynamics of the slider is negligible and will be ignored in this study. Apart from the rigid body mode, and the E-block arm modes, the actuator exhibits three types of deflection shapes. The first of these is represented by mode 3, which is called the butterfly mode because of its shape. The motion of the actuator in this mode is a bending about the z axis that resembles the first bending mode of a beam with free-free boundary conditions. The second deflection shape is represented by mode 13. The motion of the actuator in this mode is a torsion about the x axis and resembles the first torsion mode of a shaft with free-free boundary conditions. The last deflection shape is one which involves bending about the y axis and is called the fish mode because of its shape. It resembles the first bending mode (about the y axis) of a beam with free-free boundary conditions. The actuator exhibits a number of fish modes with different ‘tail’ configurations.

Actuator modes that contribute significantly to off-track motion include the rigid body rotation mode (RBM), the butterfly mode, mode 13, the two sway modes of the E-block arms (ES_1, ES_2), and the seven first torsion modes of the E-block arms (ET1). The motion of the E-block arms in some of these first torsion modes are similar, but it combines with different tail configurations in different modes. Actuator modes that contribute significantly to flying height modulation include the three first bending modes of the E-block arms, and the fish modes.

III.III. The Head Stack Assembly

When the actuator and the four HGA's are combined into the HSA model, a multitude of modes results due to the dynamic coupling between the various components. Some of these modes are listed in Table 4, and are depicted in Figs. 24 through 40. There is a shift to lower frequencies of the natural modes as compared with the natural frequencies of individual component HGA modes.

The rigid body rotation mode and the butterfly mode do not couple with HGA modes, because their natural frequencies are much lower than those of the HGA modes. The single suspension modes bifurcate, as a result of the coupling between the four suspensions, into several coupled modes that can be grouped into sets corresponding to each suspension mode. Most of these sets consist of four modes: two modes in which the two inner suspensions are vibrating (in phase in one mode and out of phase in the other) while the two outer suspensions exhibit very little motion; and two modes where the two

outer suspensions possess most of the motion (in phase in one and out of phase in the other) while the two inner suspensions have very little motion. The suspension modes also couple with some of the actuator modes.

The suspension first bending set (modes 3 through 6) covers the range 1,468.2 Hz to 1,492.5 Hz, compared with the suspension first bending at 1,570.8 Hz. The suspension first torsion set (modes 10 through 13) covers the range 2,716.9 Hz to 2,718.2 Hz, compared with the suspension first torsion at 2,889.8 Hz. The suspension second bending set (modes 17 through 20) covers the range 4,408.9 Hz to 4,463.4 Hz, compared with the suspension second bending at 4,737.5 Hz. The suspension second torsion set (modes 25 through 28) covers the range 6,774.3 Hz to 6,780.5 Hz, compared with the suspension second torsion at 7,171.5 Hz. The flexure bending set (modes 32 through 35) covers the range 7,807.6 Hz to 7,819.1 Hz, compared with the flexure bending at 8,005.1 Hz.

The coupling with the loadbeam third bending mode in these modes is more pronounced than it is in the corresponding mode of the component HGA. The suspension third bending set (modes 40 through 43) covers the range 8,915.2 Hz to 8,925.6 Hz, compared with the suspension second bending at 9,130.4 Hz. The suspension flexure torsion set (modes 46 through 49) covers the range 9,270.4 Hz to 9,406.8 Hz, compared with the flexure torsion mode at 9,535.2 Hz. This suspension mode couples with one of the E-block first torsion modes in mode 50 at 9,452.9 Hz. The suspension sway set (modes 56, 57, 58, 60, 61, and 63) covers the range 10,601 Hz to 12,049 Hz, compared with the suspension sway at 11,440 Hz. The first four of these modes are suspension modes that

hardly couple with any E-block modes. The suspension sway modes couple with some E-block arm first torsion modes in modes 61 and 63.

The suspension third torsion modes couple strongly with the E-block arm first torsion modes resulting in over ten coupled modes: modes 64 through 72 and mode 74. As a result, the suspension third torsion mode appears over a large frequency range, 12,140 Hz to 13,978 Hz, compared with the component third torsion at 13,318 Hz.

From these results, it is clear that the natural frequencies of the various HGA modes in the coupled system are lower than the natural frequencies of the corresponding modes of the individual component HGA (the results presented in §3.1). Some HGA modes are driven by certain actuator modes. As a result of this coupling and of the coupling among the four HGAs, familiar suspension modes appear over a wider frequency range. Examining the results also indicates that all the actuator modes in the frequency range considered, with the exception of the rigid body rotation mode and the butterfly mode, invariably drive and couple with some HGA modes. The rigid body rotation and butterfly modes do not couple with the HGA modes because their natural frequencies are considerably lower than those of the HGA modes. On the other hand, many of the modes in the various sets exhibit mode shapes with significant deformations in the HGAs only, and practically negligible deformations in the rest of the system. This suggests that HGA modes do not necessarily drive actuator modes.

Fig. 41 depicts the FRF of the four sliders in the HSA representing the off-track response of the sliders to a unit rotational excitation at the E-block pivot (about the pivot axis). The modes excited are again mostly modes that contribute to off-track motion. The FRFs are clearly denser with modes than that of the component HGA (Fig. 13). There is actually over 40 coupled HGA and actuator modes in the 14 kHz frequeny range, compared with the five modes of Fig. 13.

IV. Conclusions

The dynamics of a two-disk HSA were investigated using finite element analysis at the component level and at the system level. The main components of the HSA are the HGAs and the actuator. The components and the assembled system were studied, and structural modes that contribute to off-track vibration and those that contribute to flying height variation were identified.

The results illustrate that suspension modes occur at lower natural frequencies in the HSA than in the single HGA model. The single HGA modes bifurcate, as a result of the coupling among the four HGAs, into several coupled modes that can be grouped into sets corresponding to each suspension mode. Most of these sets consist of four modes: two modes in which the two inner suspensions are vibrating while the two outer suspensions exhibit very little motion, and two modes where the outer suspensions possess most of the motion while the inner suspensions have very little motion. Some HGA modes are driven by certain actuator modes. As a result of this coupling and of the coupling among the four HGAs, familiar suspension modes appear over a wide frequency range. The results also demonstrate that, with the exception of the rigid body rotation and the butterfly modes, the actuator modes invariably drive and couple with some HGA modes, whereas the HGA modes do not necessarily drive actuator modes.

The FRFs of the sliders in the HSA model are far denser in modes than that of the component HGA, and the response calculated using the HSA FRF is expected to be

appreciably greater than that calculated using the FRF of a single HGA or even that of a single arm single suspension assembly.

This study demonstrates a variety of effects that arise as a result of the coupling of the HSA components. With the decrease in the allowable vibration budgets and increase in the sources of excitation, such effects can no longer be considered negligible. Disk drive dynamics must be addressed at the system level if higher track densities and lower flying heights are to be achieved.

V. References

1. Yoshida, T., Hirai, H., et al., “Vibration Reduction of a Small Magnetic Disk Drive Using a Nonreacting, Twin-Drive Actuator”, ASME, Advances in Information Storage Systems, Vol. 6, 1995, pp. 289-300.

2. Ku, C. P. R., “Dynamic Characteristics of Hard Disk Drive Spindle Motors Comparison Between Ball Bearings and Hydrodynamic Bearings”, ASME, Journal of Tribology, Vol. 118 (2), April 1996, pp. 402-406.

3. McAllister, J. S., “The Effect of Platter Resonances on Track Misregistration in Disk Drives”, Journal of Sound and Vibration, January 1996, pp. 24-28.

4. Zeng, Q. H., and Bogy, D. B., “Experimental Modal Analysis Technique, System and Application for Miniature Structures”, CML Report No. 96-011, Computer Mechanics Laboratory, Department of Mechanical Engineering, University of California at Berkeley, May, 1996.

5. Radwan, H. R., and Whaley, R., “Servo Structural Interaction in Disk Drives Using Finite Element Analysis”, ASME, Advances in Information Storage Systems, Vol. 5, 1993, pp. 101-118.

6. Wilson, C. J., and Bogy, D. B., “Modal Analysis of a Miniaturize Structures with Application to Components in Magnetic Recording Disk Drives”, CML Report No. 93-004, Computer Mechanics Laboratory, Department of Mechanical Engineering, University of California at Berkeley, May, 1993.

7. Zeng, Q. H., and Bogy, D. B., “Modal Dynamics Experiment and Analysis of a Suspension Assembly Used in Hard Disk Drives”, CML Report No. 96-013, Computer Mechanics Laboratory, Department of Mechanical Engineering, University of California at Berkeley, June, 1996.

8. Zeng, Q. H., and Bogy, D. B., “An Investigation of the Dynamic Characteristics of a Hard Disk Drive by Experiment and Analysis”, CML Report No. 96-017, Computer Mechanics Laboratory, Department of Mechanical Engineering, University of California at Berkeley, August, 1996.

9. Williams, D., and Balasingam, S., “Why Rotary Actuators Behave the Way They Do”, Data Storage, November/December 1995, pp. 43-48.

Material	Young's Modulus [GPa]	Density [kg/m^3]	Poisson's Ratio
Stainless Steel	190	8072	0.32
Beam Material	393	0	0.23
Aluminum 6061-T6	69	2710	0.33
Aluminum	70	2710	0.33
Overmold Material	0.1	1650	0.00

Table 1: Material properties used in finite element modeling

Mode	Natural Frequency [Hz]	Mode Shape
1	1570.8	Suspension first bending
2	2889.8	Suspension first torsion
3	4737.5	Suspension second bending
4	7171.5	Suspension second torsion
5	8005.1	Flexure bending
6	9130.4	Suspension third bending
7	9535.2	Flexure torsion coupled with suspension second torsion
8	11440	Suspension sway
9	13318	Suspension third torsion

Table 2: Natural frequencies and associated mode shapes of the HGA

Mode	Natural Frequency [Hz]	Mode Shape
1	59.59	Rigid body rotation mode
3	1709.5	Butterfly mode
5	2412.2	E-block arm first bending 1
6	2869.9	E-block arm first bending 2
7	3108.5	E-block arm first bending 3
13	6812.4	Free-free torsion about x axis
17	8844.8	Fish mode 1
19	9127.1	Fish mode 2
20	9451.5	Fish mode 3
21	9588.3	Fish mode 4
22	9866.4	E-block arm sway 1
26	11146	E-block arm first torsion 1
27	11275	E-block arm sway 2
29	11720	E-block arm first torsion 1
31	12042	E-block arm first torsion 2
32	12143	E-block arm first torsion 3
34	12662	E-block arm first torsion 4
36	13497	E-block arm first torsion 5
37	13858	E-block arm first torsion 6
38	13917	E-block arm first torsion 7

Table 3: Natural frequencies and associated mode shapes of the actuator

Mode	Natural Frequency [Hz]	Mode Shape
1	57.974	Rigid body rotation mode
3	1468.2	Suspension first bending 1
4	1482.9	Suspension first bending 2
5	1484.7	Suspension first bending 3
6	1492.5	Suspension first bending 4
7	1670.4	Butterfly
9	2360.1	E-block arm first bending 1
10	2716.9	Suspension first torsion 1
11	2717.5	Suspension first torsion 2
12	2717.6	Suspension first torsion 3
13	2718.2	Suspension first torsion 4
14	2800.1	E-block arm first bending 2
15	3035.8	E-block arm first bending 3
17	4408.9	Suspension second bending 1
18	4435.1	Suspension second bending 2
19	4450.9	Suspension second bending 3
20	4463.4	Suspension second bending 4
25	6774.3	Suspension second torsion 1
26	6777.3	Suspension second torsion 2
27	6778	Suspension second torsion 3
28	6780.5	Suspension second torsion 4
29	6803.7	Suspension second torsion coupled with E-block mode 13
32	7807.6	Flexure bending 1
33	7810.6	Flexure bending 2
34	7816.8	Flexure bending 3
35	7819.1	Flexure bending 4
37	8437.4	Suspension sway 1
38	8517.4	Suspension sway 2
39	8812.4	Suspension third bending coupled with E-block fish mode
40	8915.2	Suspension third bending 1
41	8921	Suspension third bending 2

Table 4: Natural frequencies and associated mode shapes of the HSA

Mode	Natural Frequency [Hz]	Mode Shape
42	8924.6	Suspension third bending 3
43	8925.6	Suspension third bending 4
45	9121.3	Suspension third bending coupled with E-block fish mode
46	9270.4	Flexure torsion coupled with suspension second torsion (1)
47	9280.8	Flexure torsion coupled with suspension second torsion (2)
48	9386.6	Flexure torsion coupled with suspension second torsion (3)
49	9406.8	Flexure torsion coupled with suspension second torsion (4)
50	9452.9	Flexure torsion coupled with suspension second torsion and E-block fish mode
56	10601	Suspension sway 1
57	10914	Suspension sway 2
58	11218	Suspension sway 3
60	11602	Suspension sway 4
61	11739	Suspension sway coupled with E-block first torsion
63	12049	Suspension sway coupled with E-block first torsion
64	12140	Suspension third torsion coupled with E-block first torsion
65	12494	Suspension third torsion coupled with E-block first torsion
66	12607	Suspension third torsion coupled with E-block first torsion
67	12748	Suspension third torsion 1
68	12950	Suspension third torsion 2
69	13084	Suspension third torsion 3
70	13115	Suspension third torsion coupled with E-block first torsion
71	13117	Suspension third torsion 4
72	13516	Suspension third torsion coupled with E-block first torsion
74	13978	Suspension third torsion coupled with E-block first torsion

Table 4 (continued): Natural frequencies and associated mode shapes of the HAS

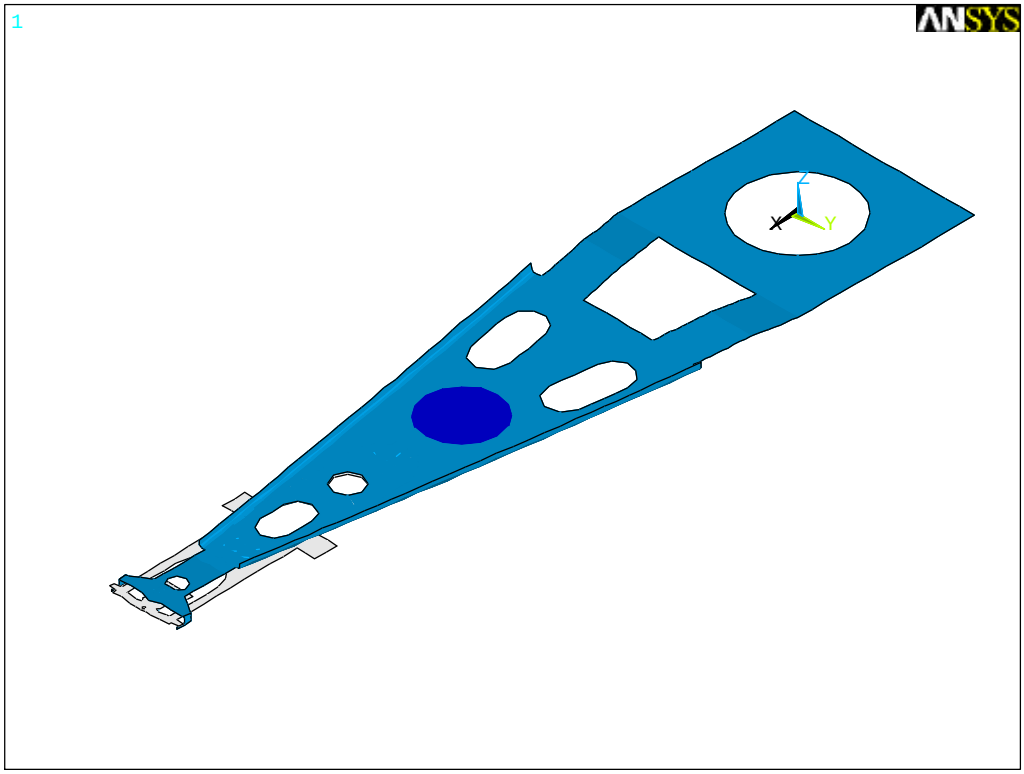

Figure 1: Solid model of HGA

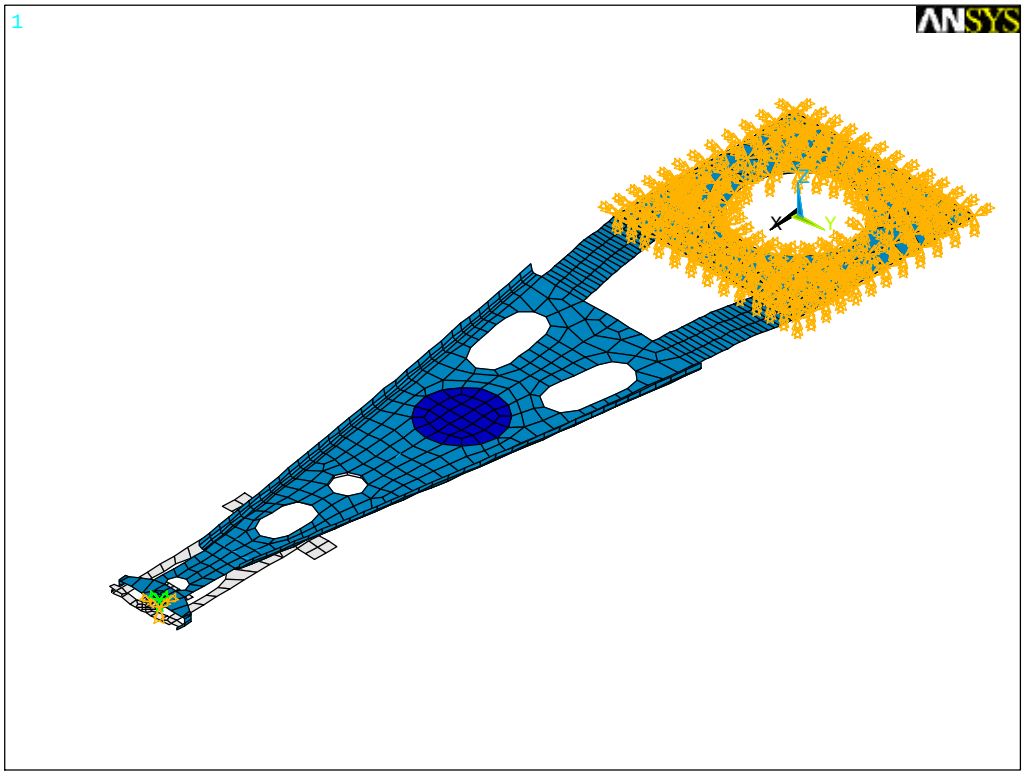

Figure 2: Finite Element model of HGA

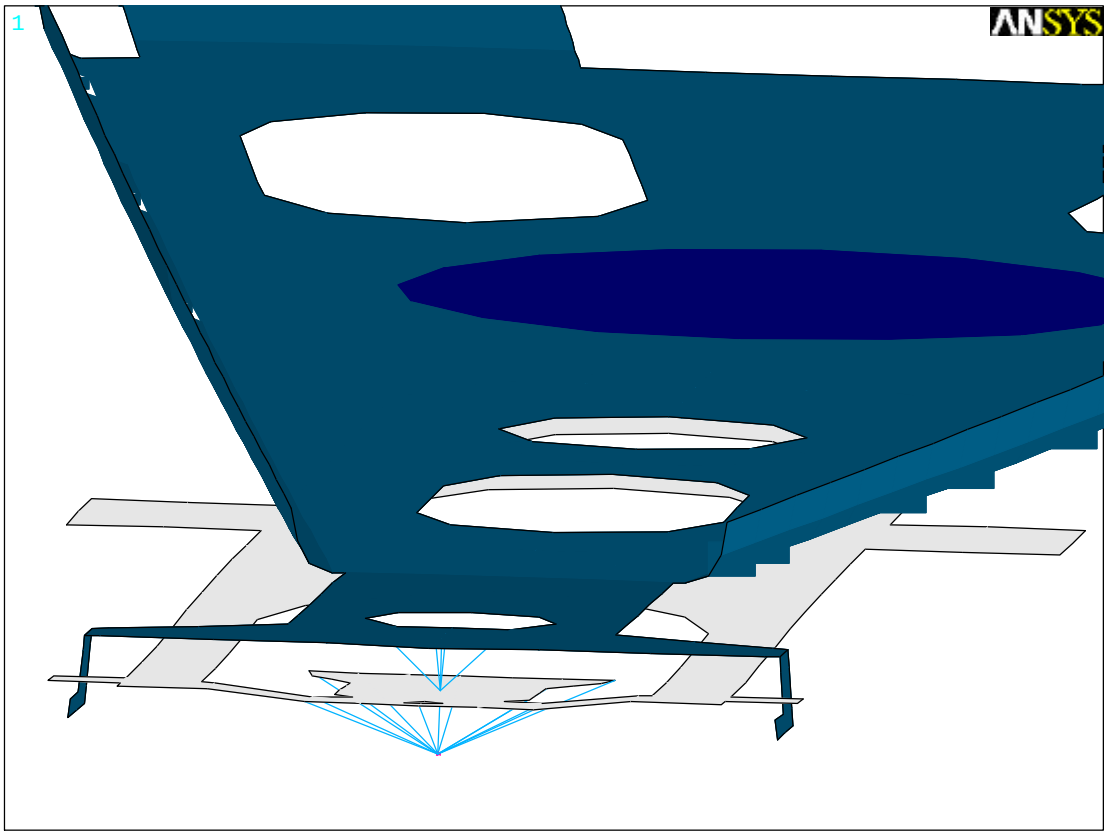

Figure 3: Close-up around the slider mass point

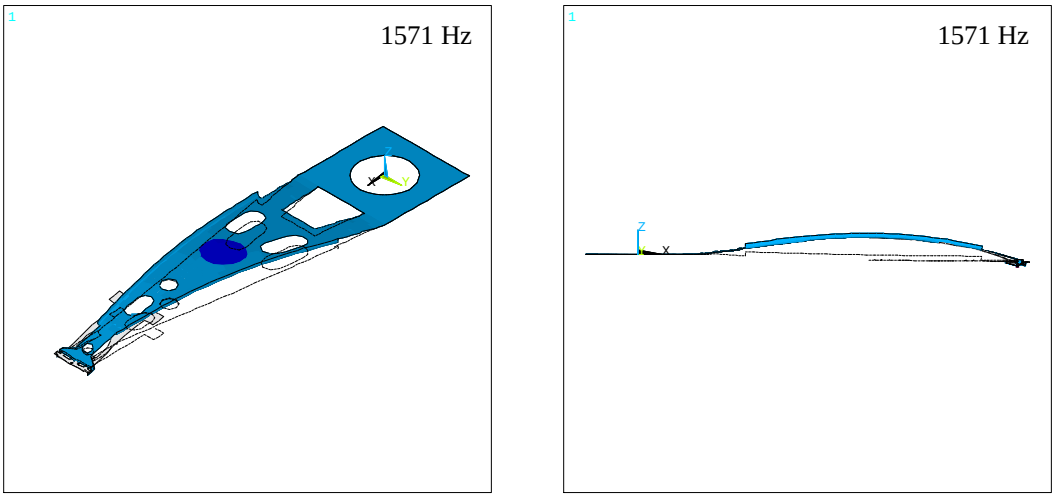

Figure 4: First bending; isometric and top views

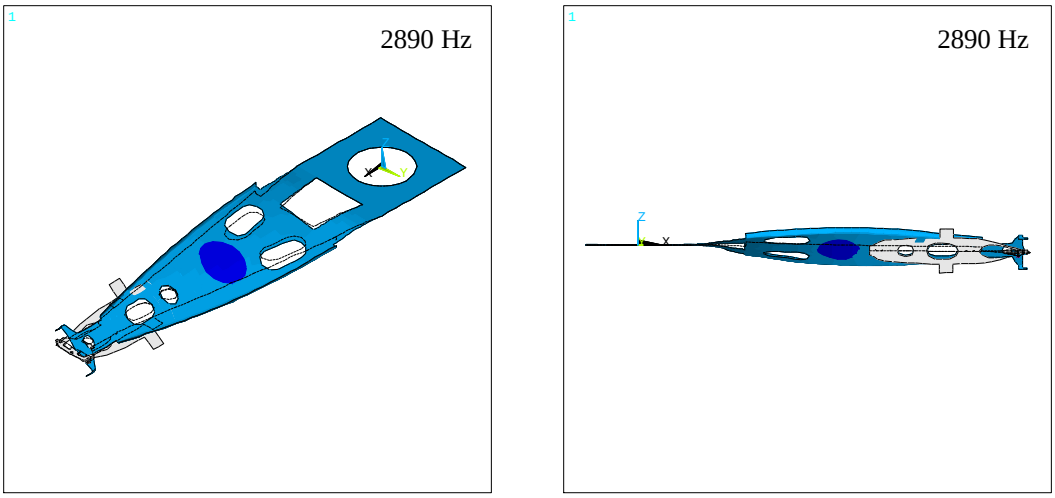

Figure 5: First torsion; isometric and top views

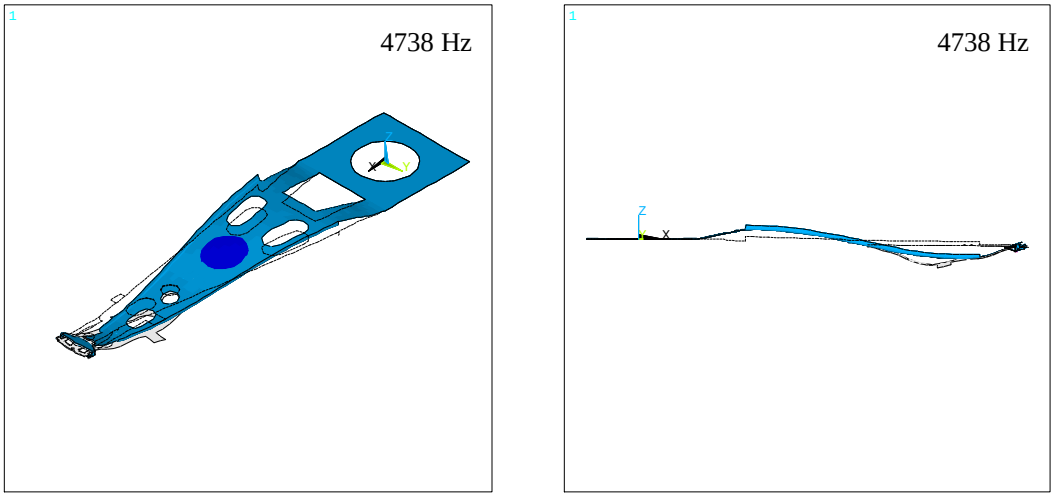

Figure 6: Second bending; isometric and top views

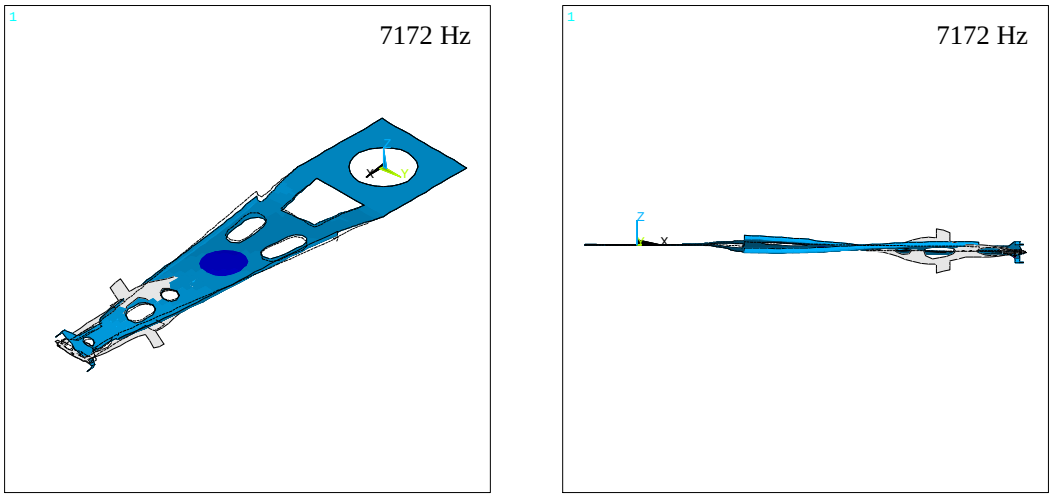

Figure 7: Second torsion; isometric and top views

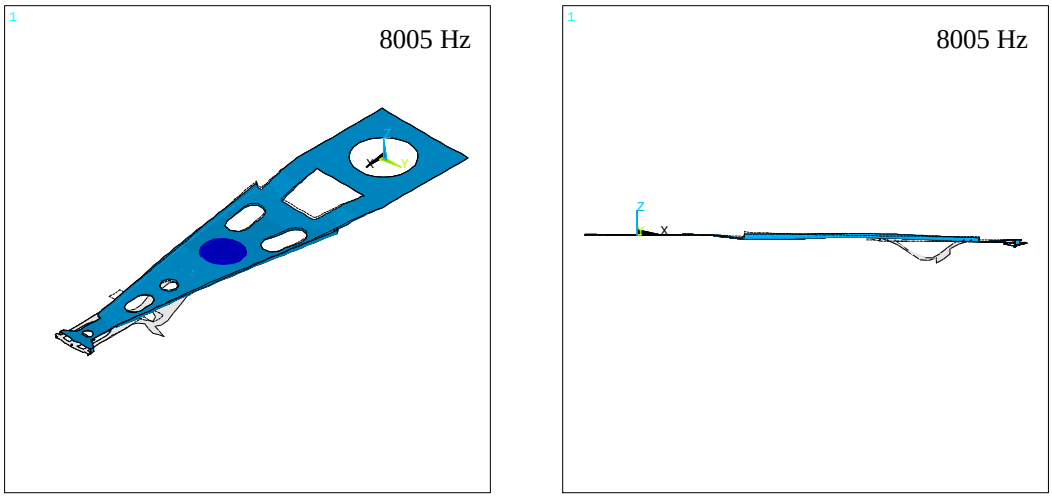

Figure 8: Flexure bending; isometric and top views

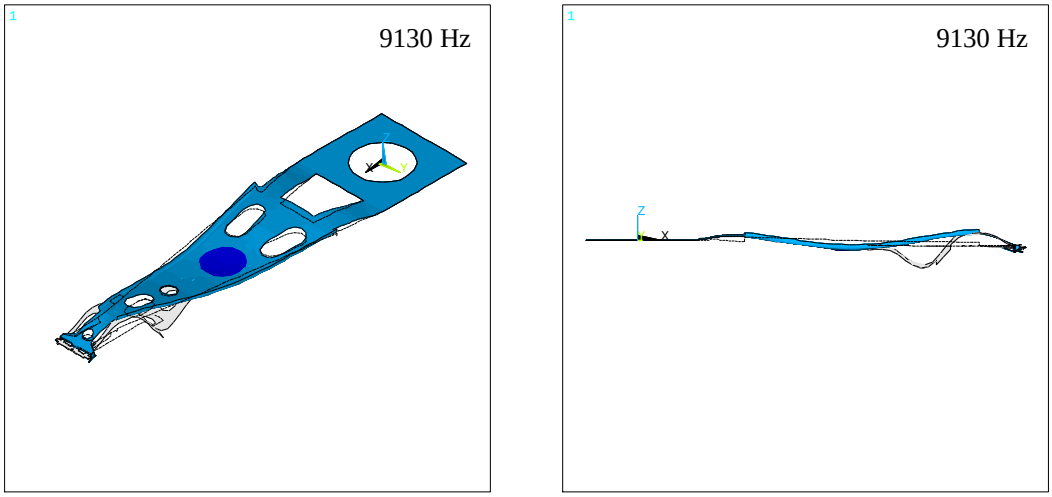

Figure 9: Third bending; isometric and top views

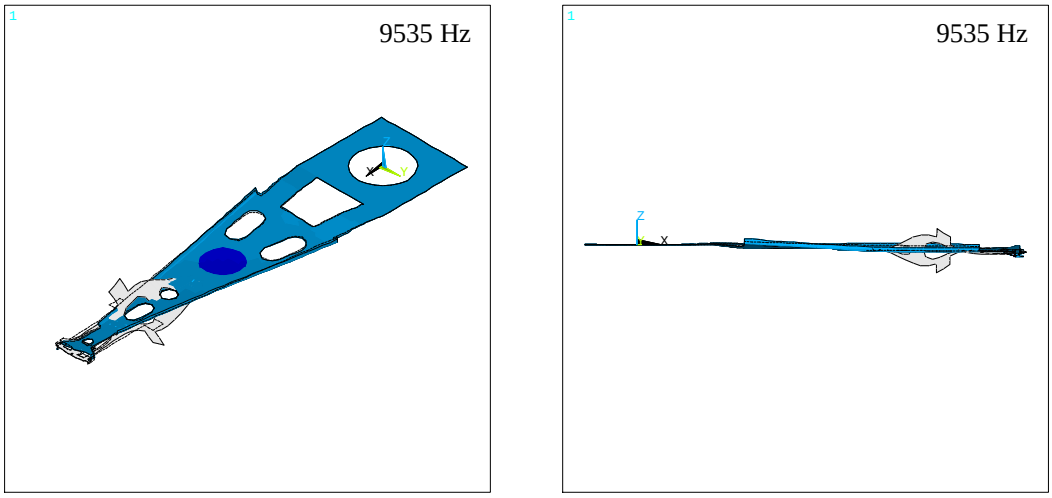

Figure 10: Second torsion coupled with flexure torsion; isometric and top views

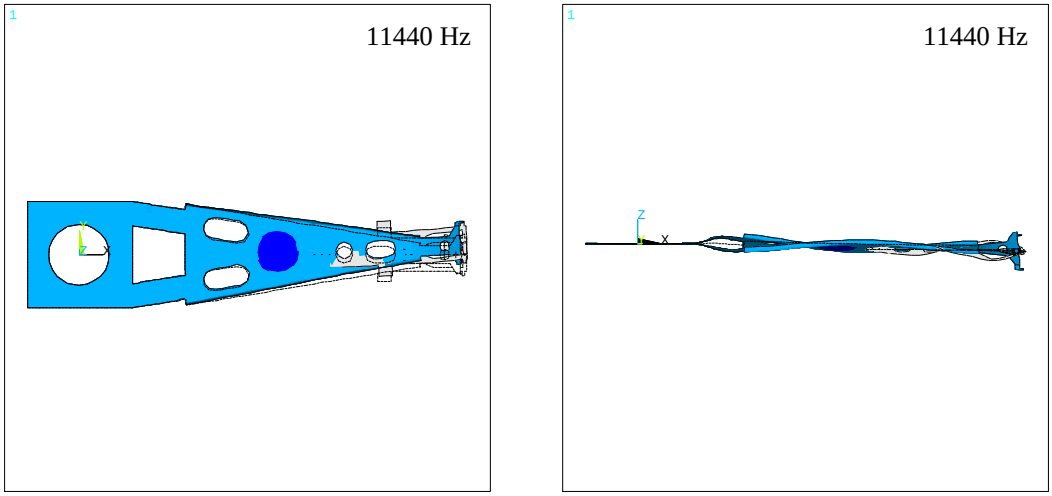

Figure 11: Sway; isometric and top views

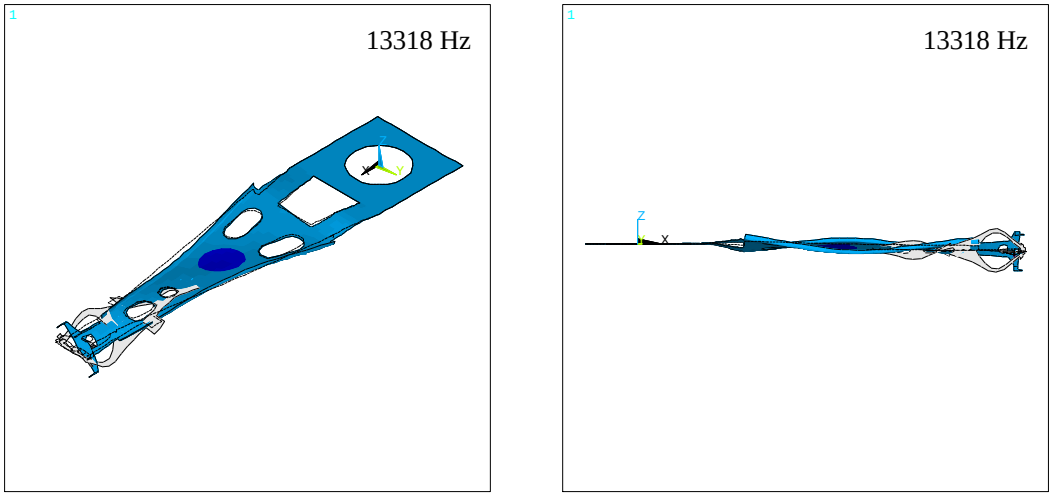

Figure 12: Third Torsion; isometric and top views

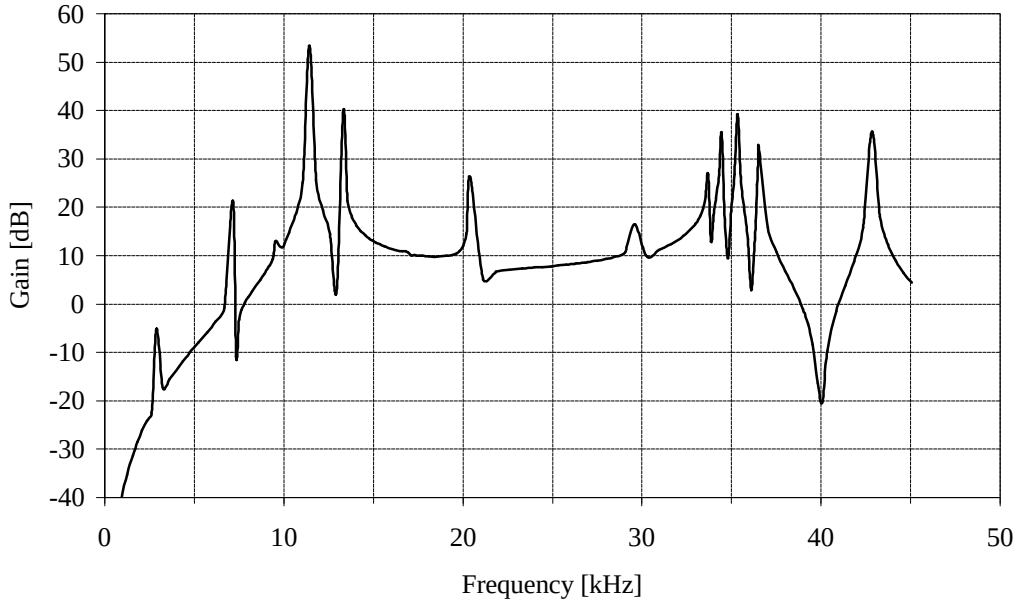

Figure 13: FRF of HGA: response at the slider to a unit lateral excitation at the baseplate

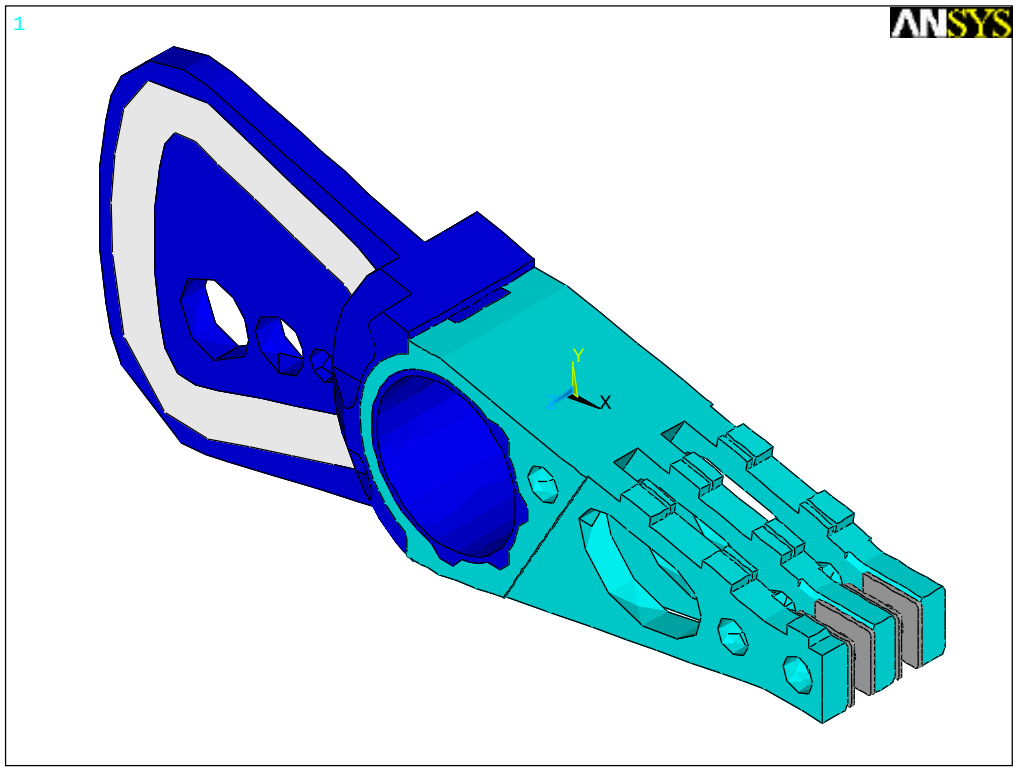

Figure 14: Solid model of E-block

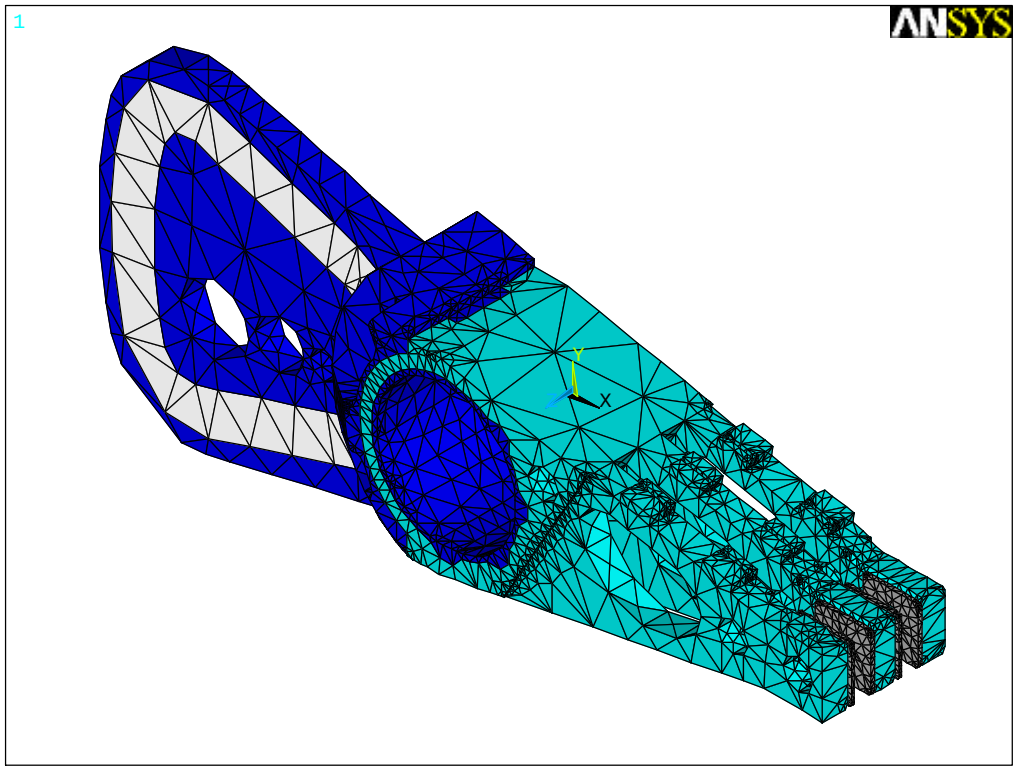

Figure 15: Finite Element model of HGA

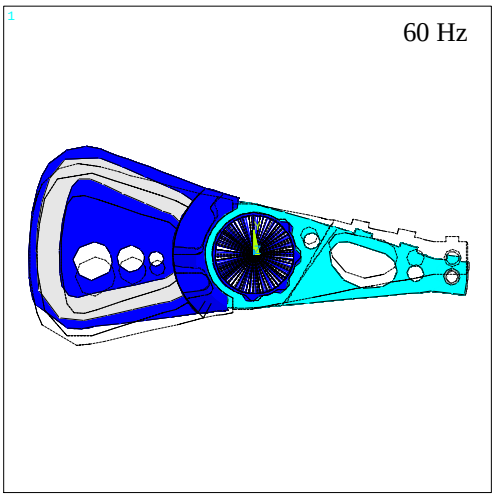

Figure 16: Rigid body rotation mode

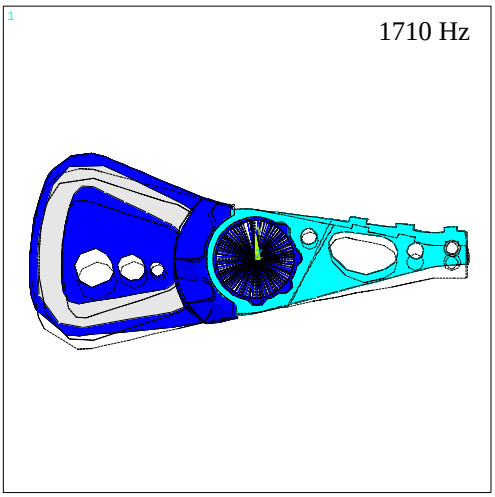

Figure 17: Butterfly mode

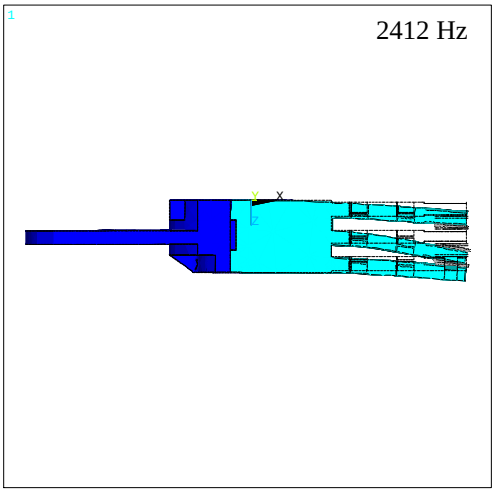

(a)

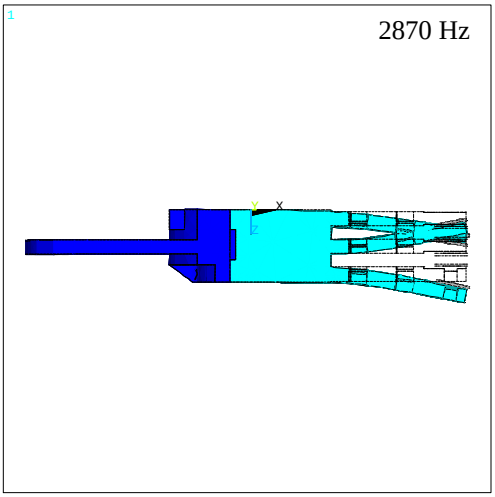

(b)

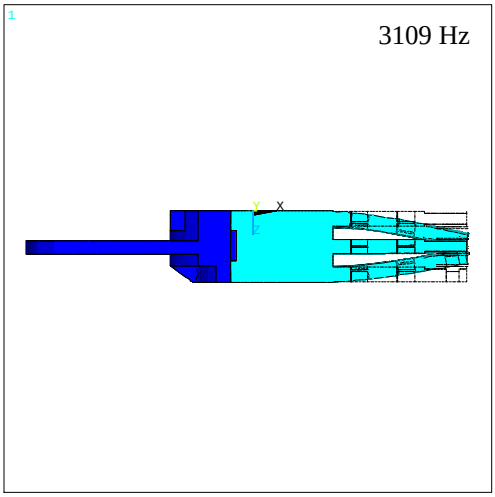

(c)

Figure 18: Three first bending modes of the E-block arms

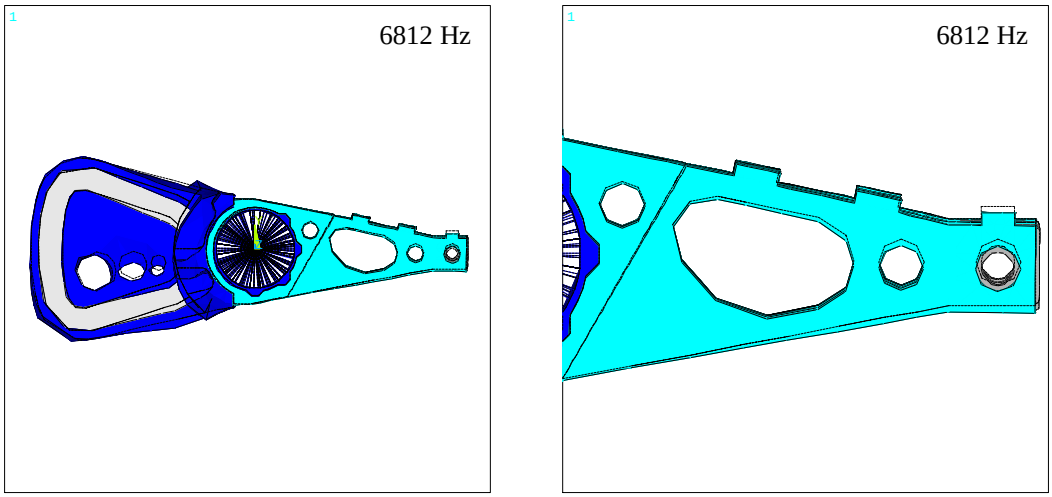

Figure 19: Mode 13; front view and close-up

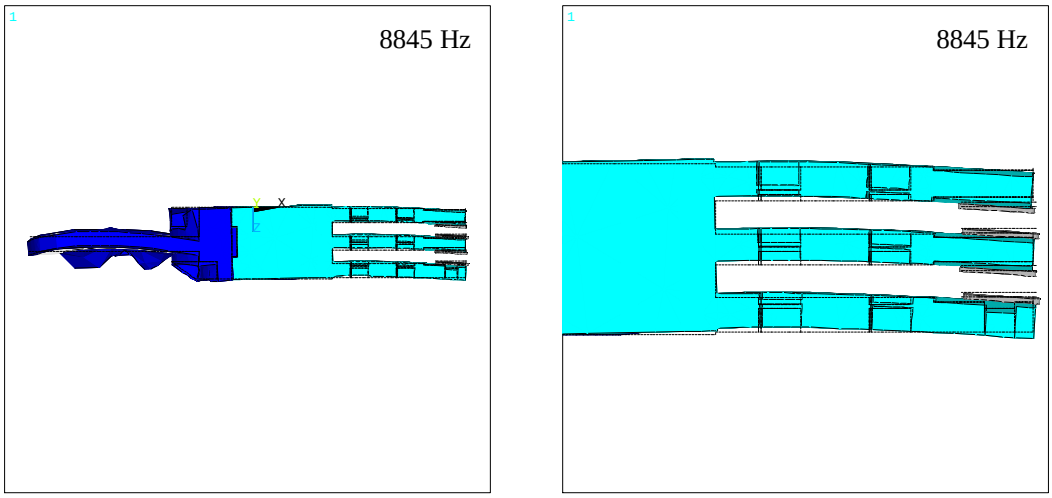

Figure 20: Fish mode; top view and close-up

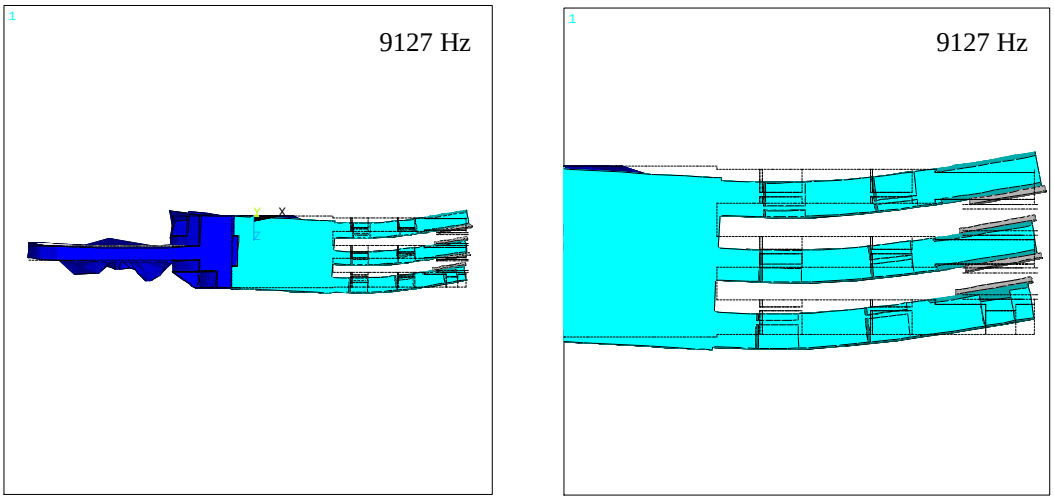

Figure 21: Fish mode; top view and close-up

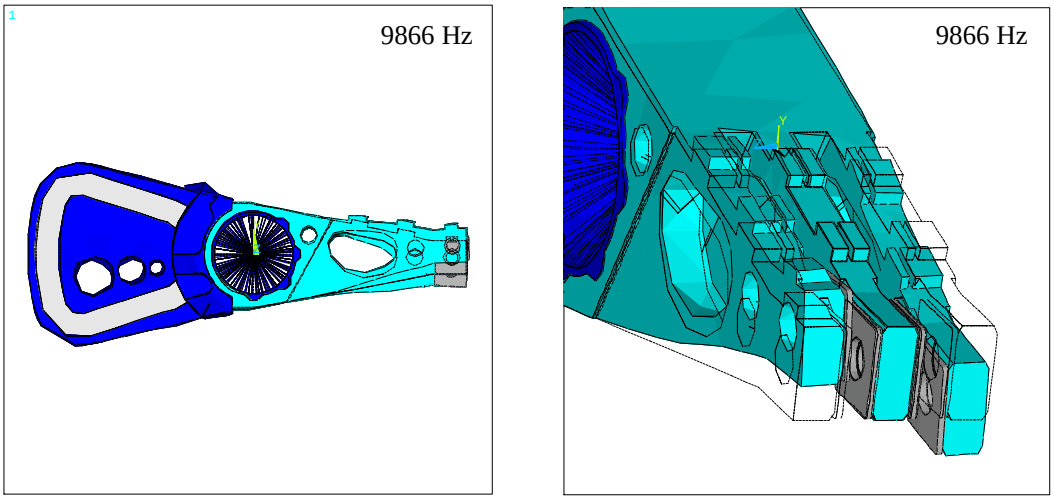

(a) mode 22: front and isometric views

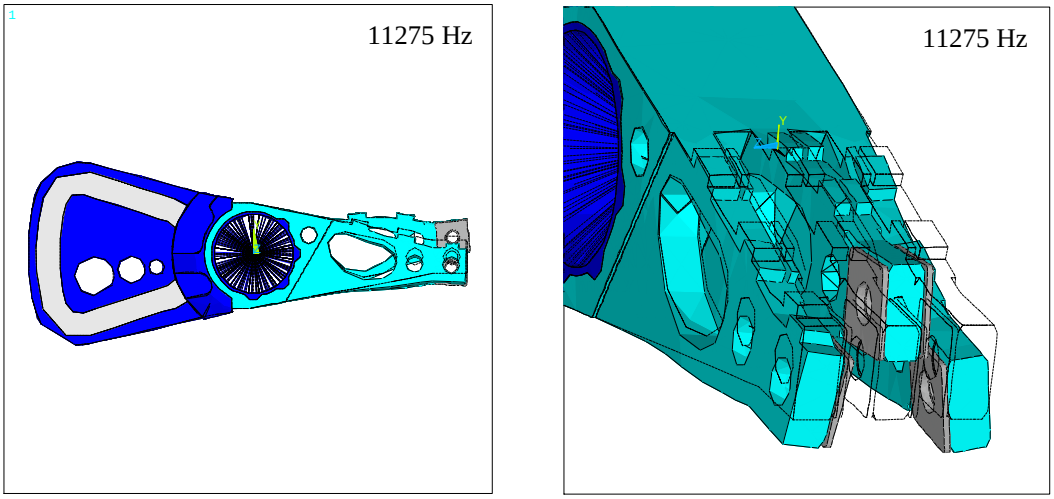

(b) mode 27: front and isometric views

Figure 22: Two sway modes of the E-block arms

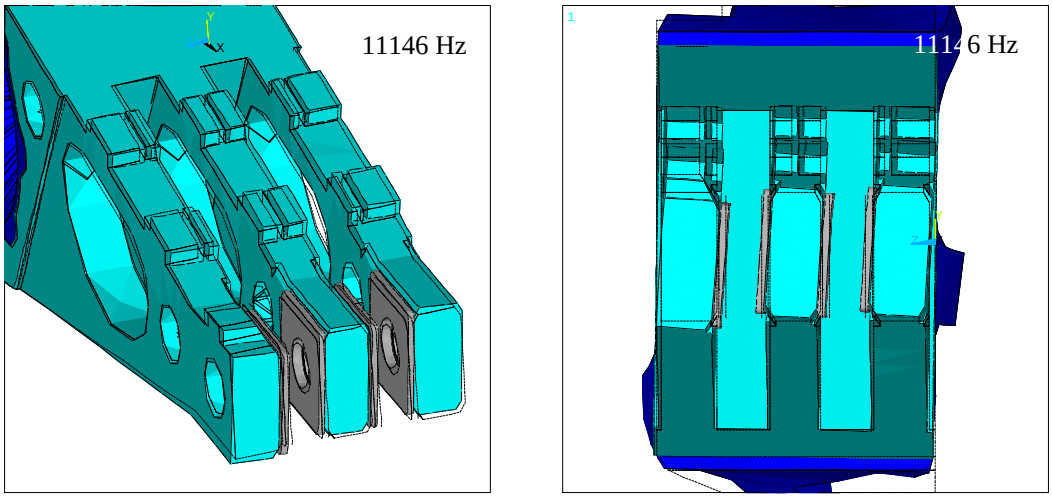

(a) mode 26: isometric and side views

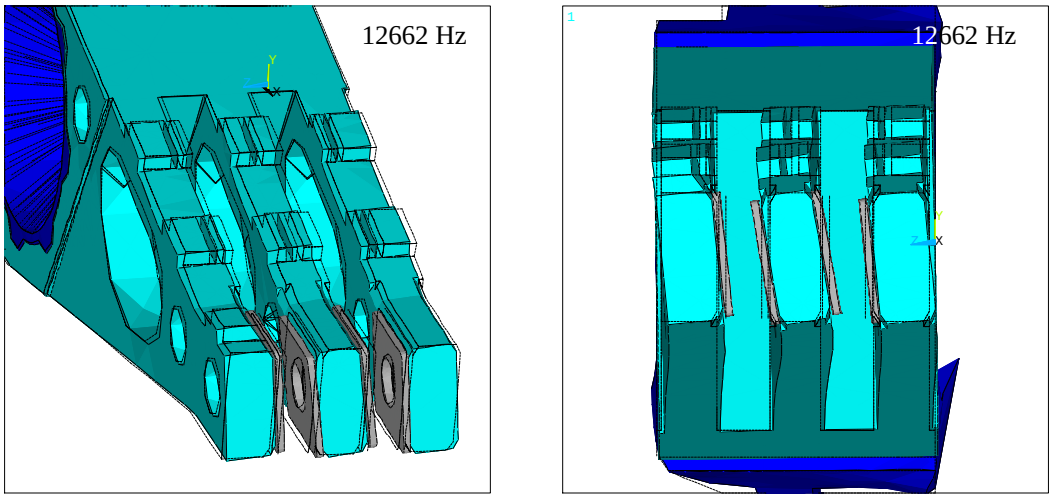

(b) mode 34: isometric and side views

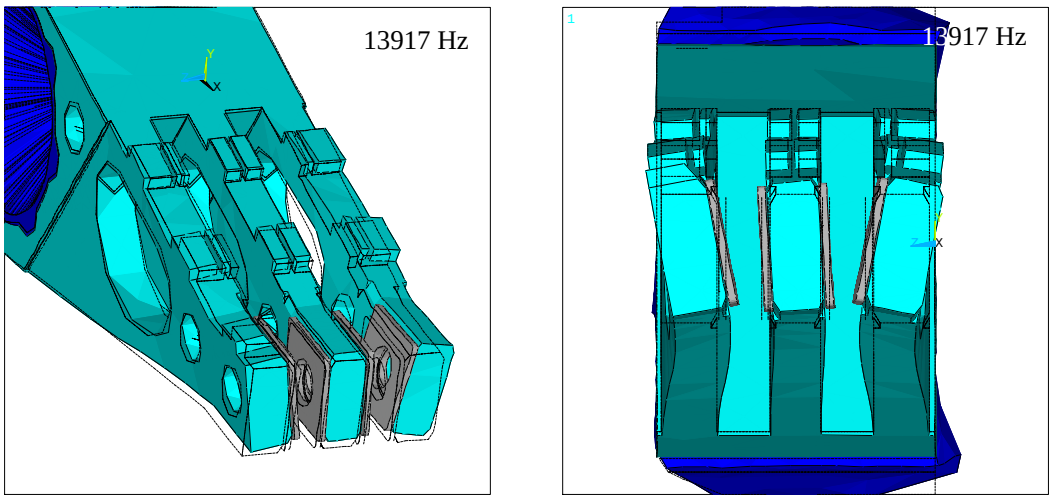

(c) mode 38: isometric and side views

Figure 23: Three first torsion modes of the E-block arms

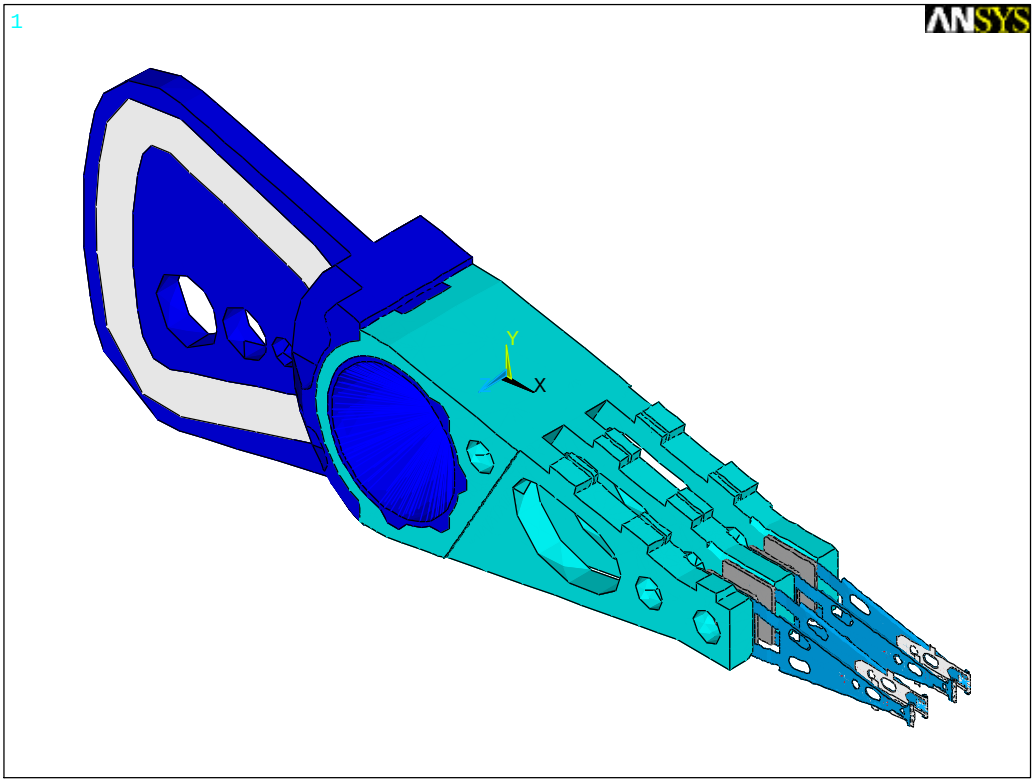

Figure 24: Solid model of HSA

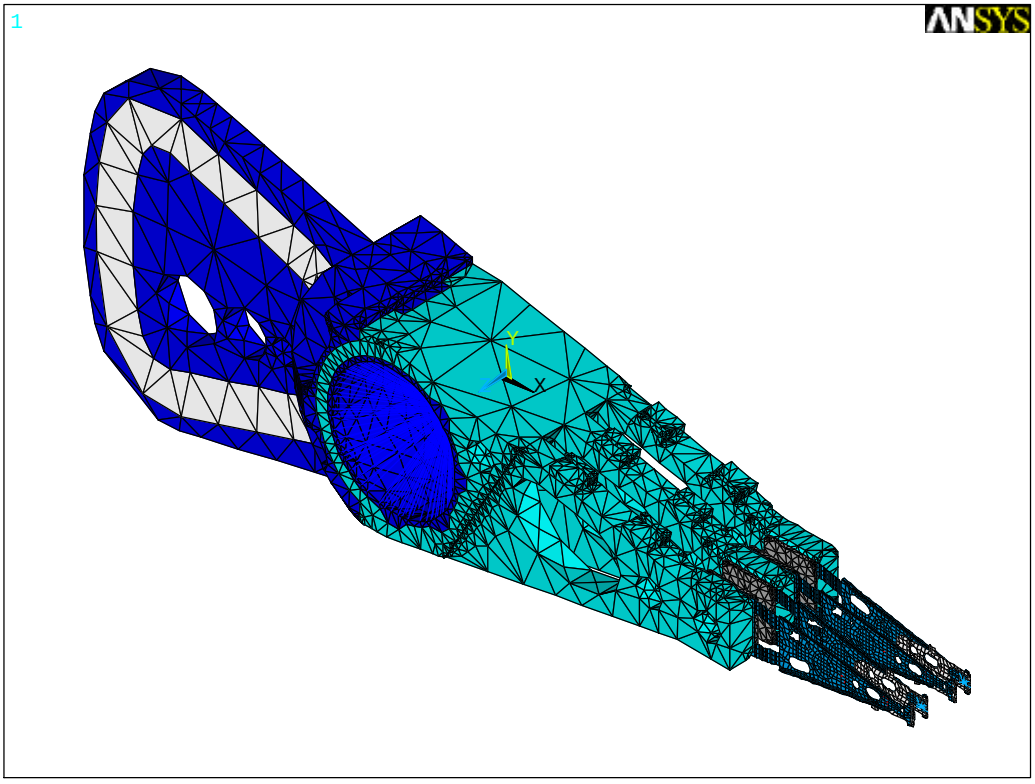

Figure 25: Finite Element model of HSA

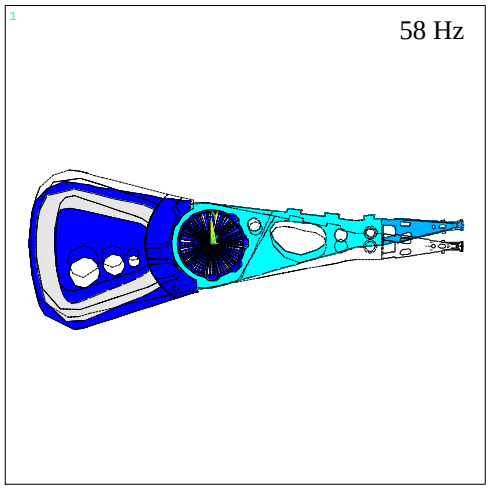

Figure 26: Rigid body rotation mode

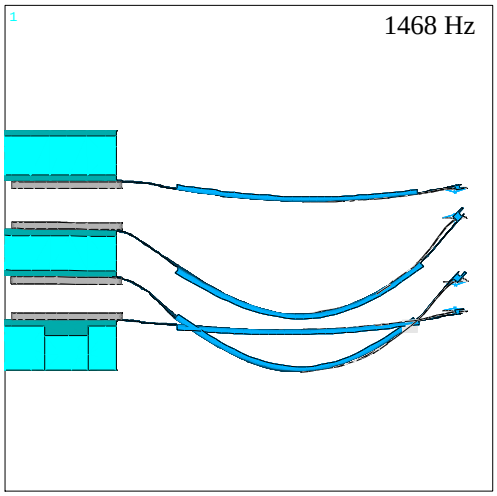

(a) Mode 3

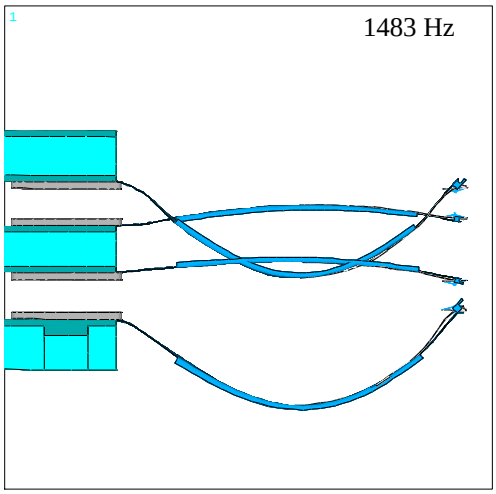

(b) Mode 4

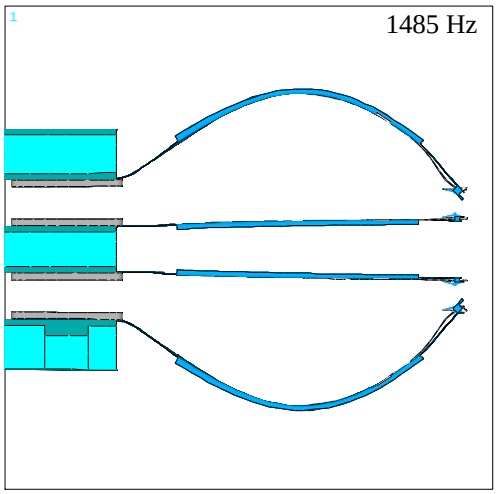

(c) Mode 5

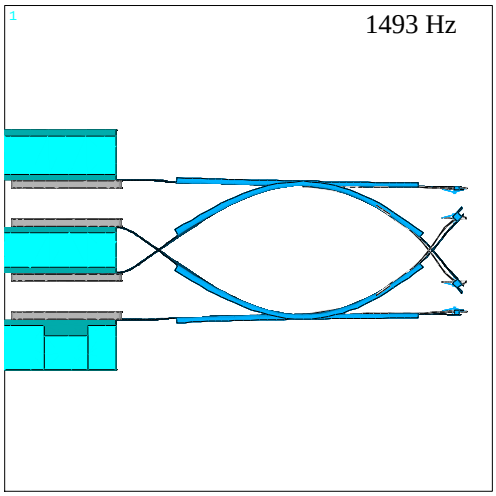

(d) Mode 6

Figure 27: Four suspension first bending modes

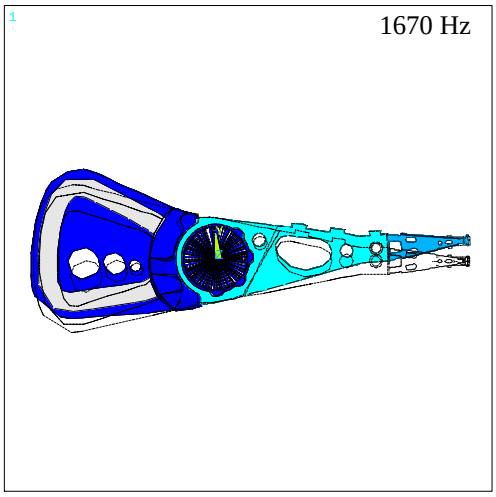

Figure 28: Butterfly mode

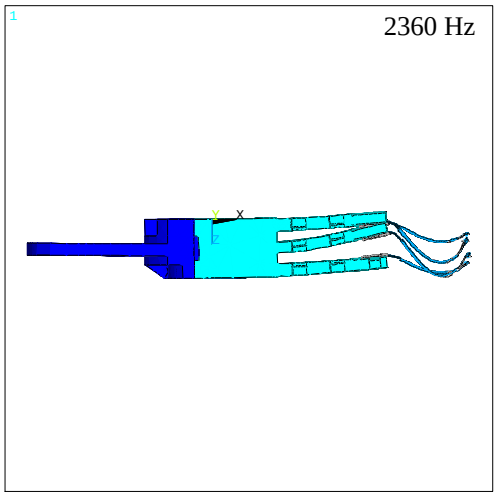

(a) Mode 9

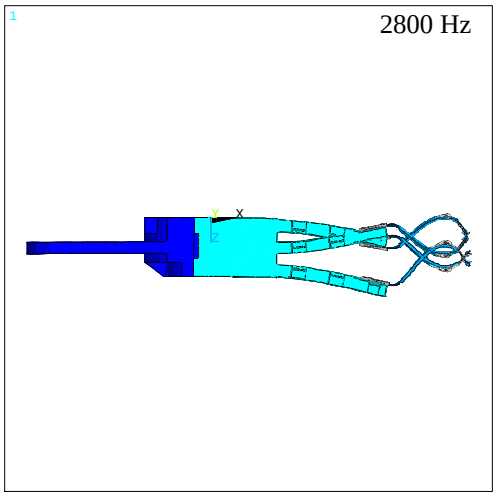

(b) Mode 14

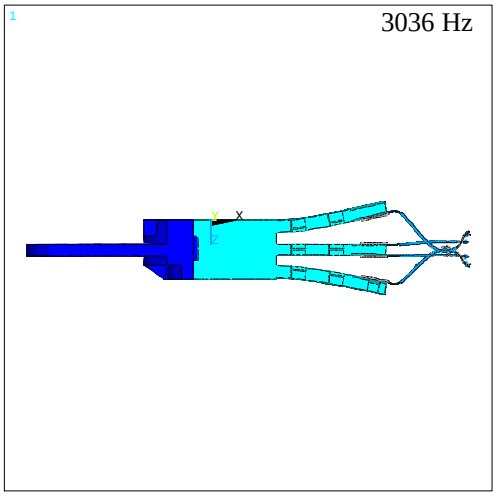

(c) Mode 15

Figure 29: Three E-block arm first bending modes

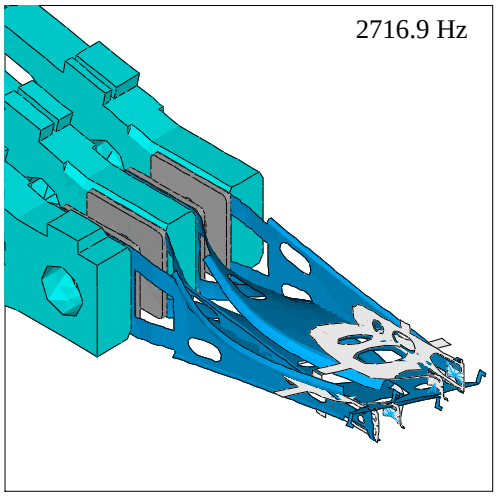

(a) Mode 10

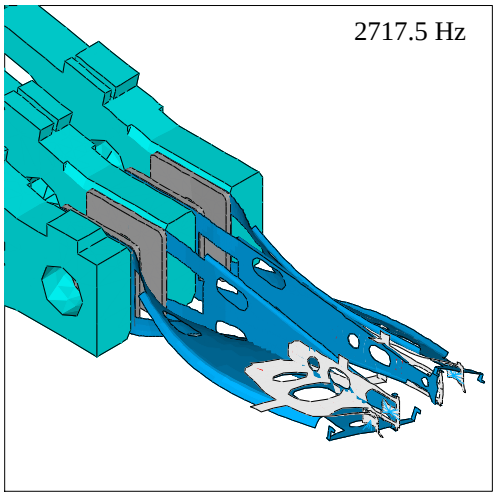

(b) Mode 11

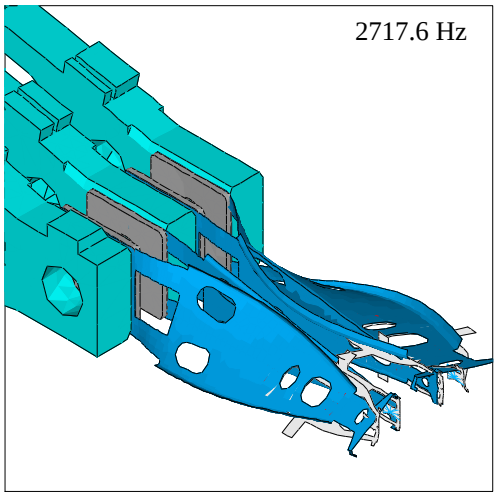

(c) Mode 12

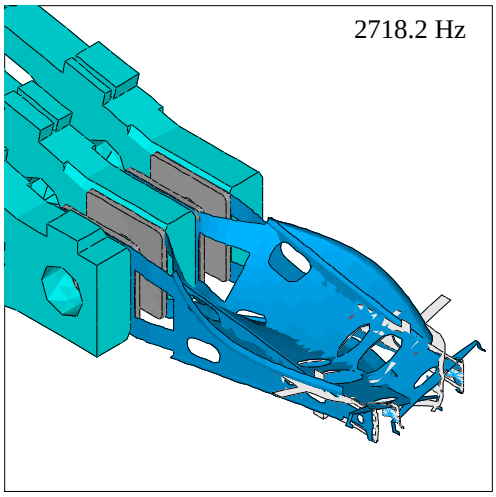

(d) Mode 13

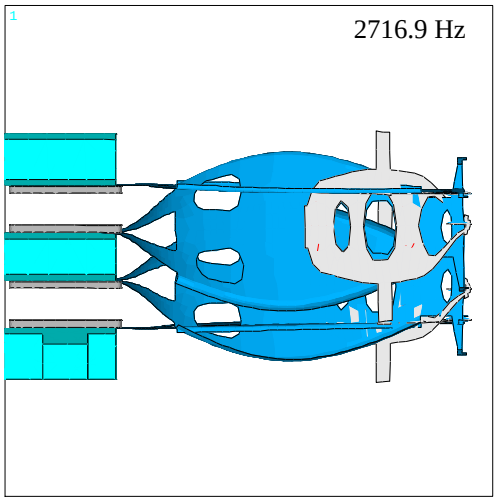

(e) Mode 10 : top view

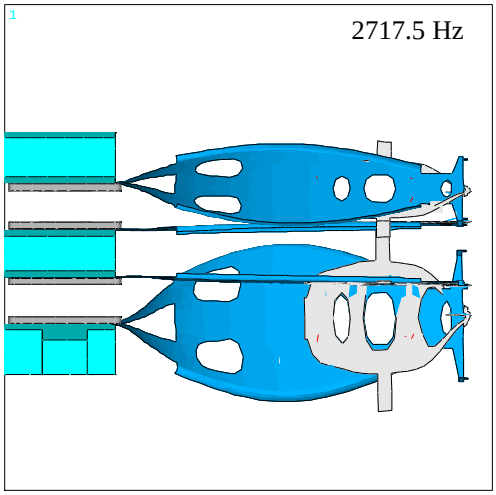

(f) Mode 11: top view

Figure 30: Four suspension first torsion modes

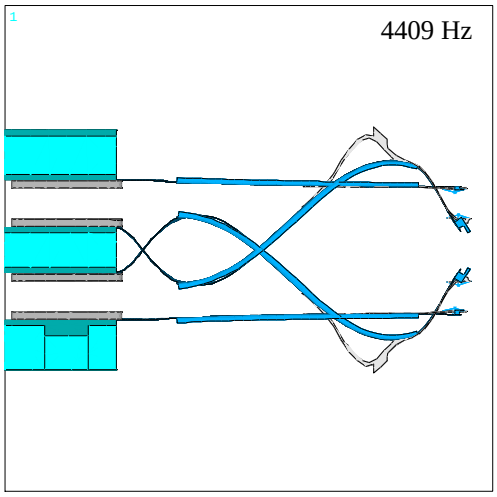

(a) Mode 17

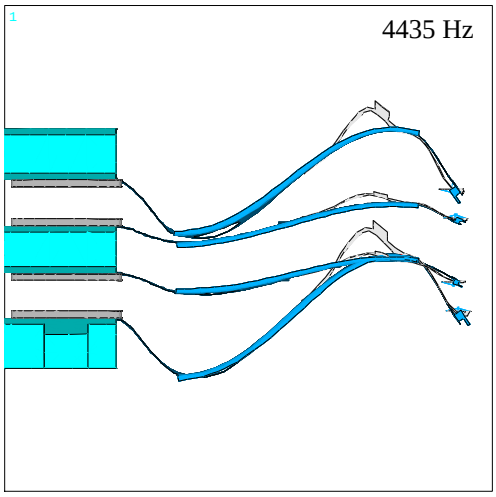

(b) Mode 18

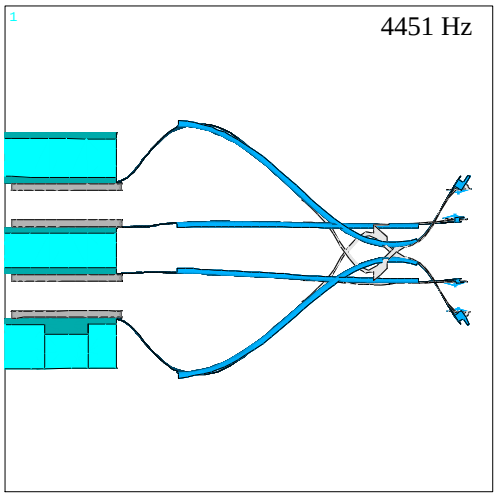

(c) Mode 19

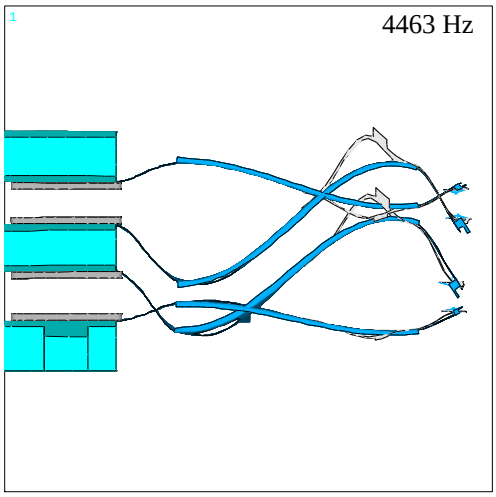

(d) Mode 20

Figure 31: Four suspension second bending modes

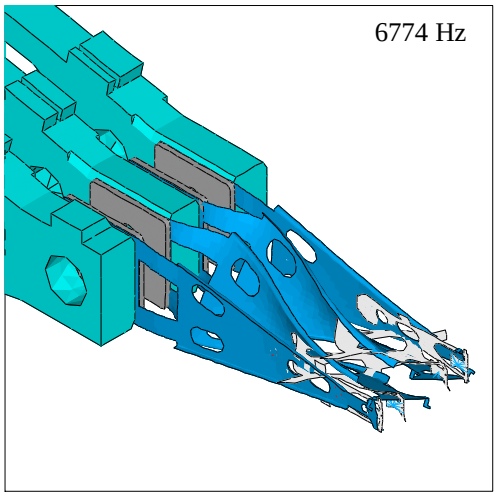

(a) Mode 25

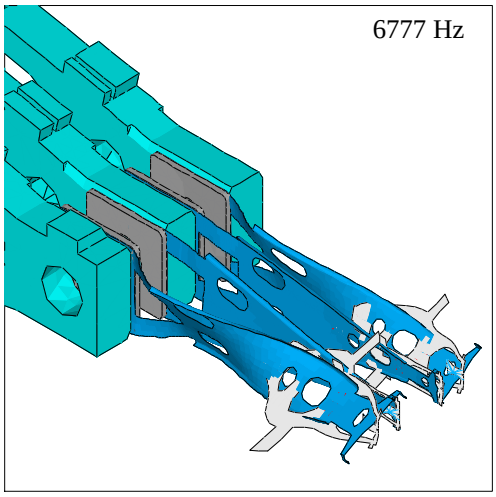

(b) Mode 26

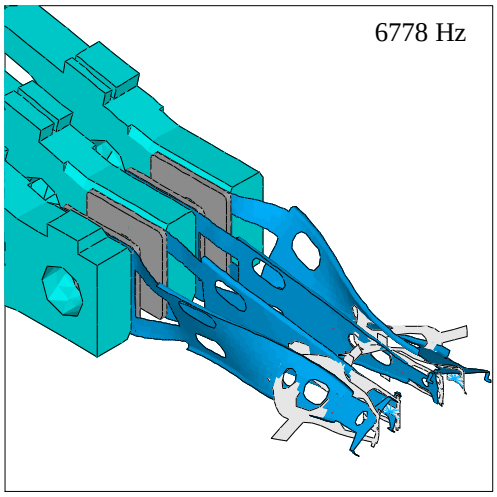

(c) Mode 27

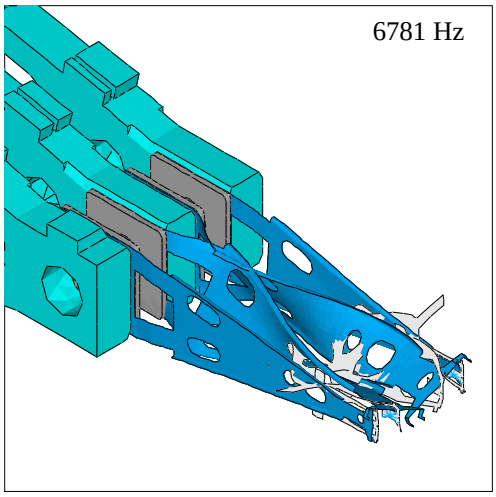

(d) Mode 28

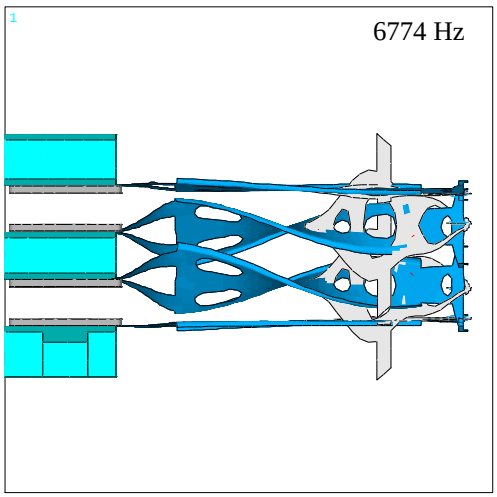

(e) Mode 25: top view

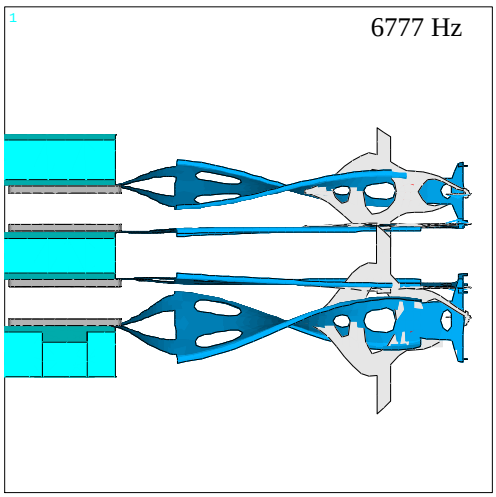

(f) Mode 26: top view

Figure 32: Four suspension second torsion modes

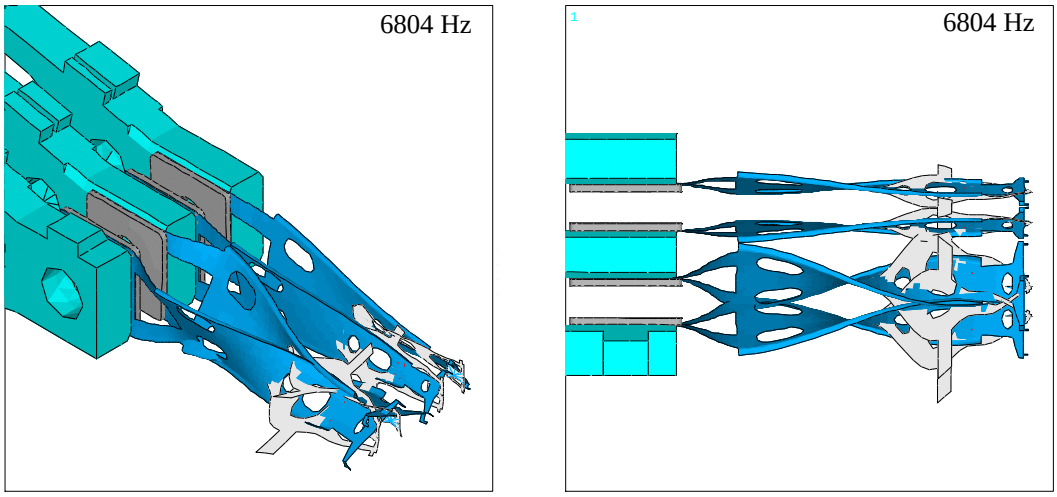

Figure 33: Suspension second torsion coupled with E-block mode 13

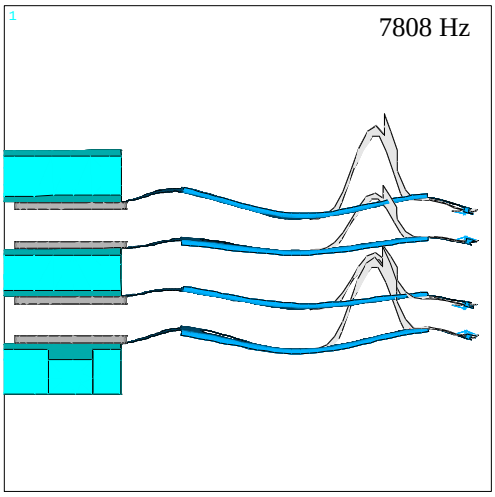

(a) Mode 32

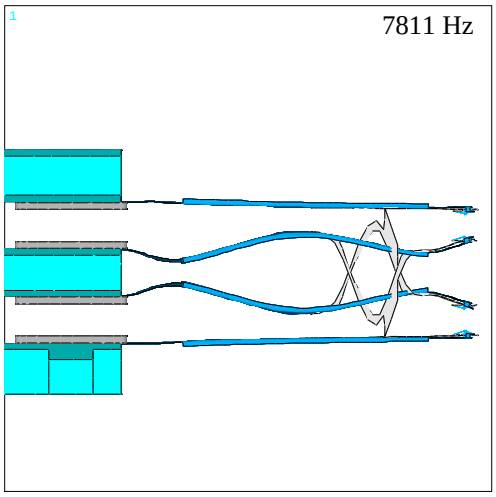

(b) Mode 33

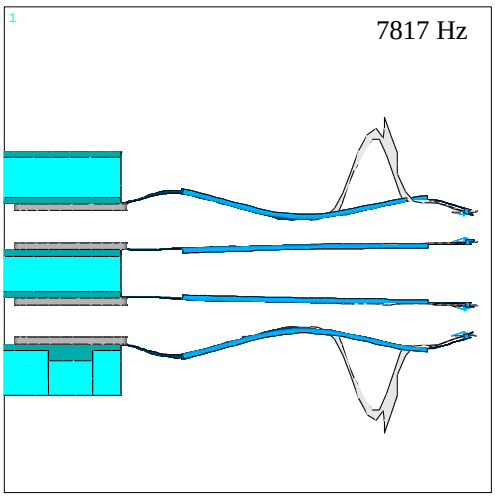

(c) Mode 34

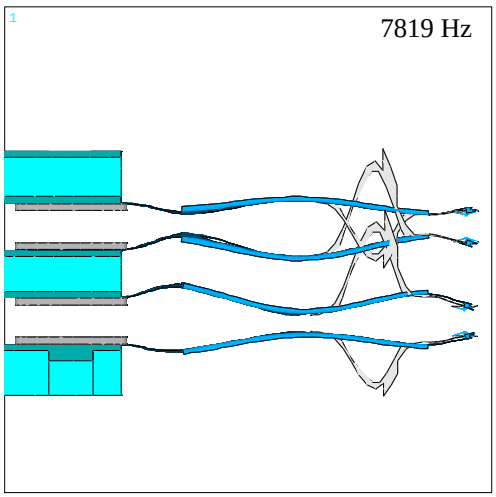

(d) Mode 35

Figure 34: Four flexure bending/suspension third bending modes

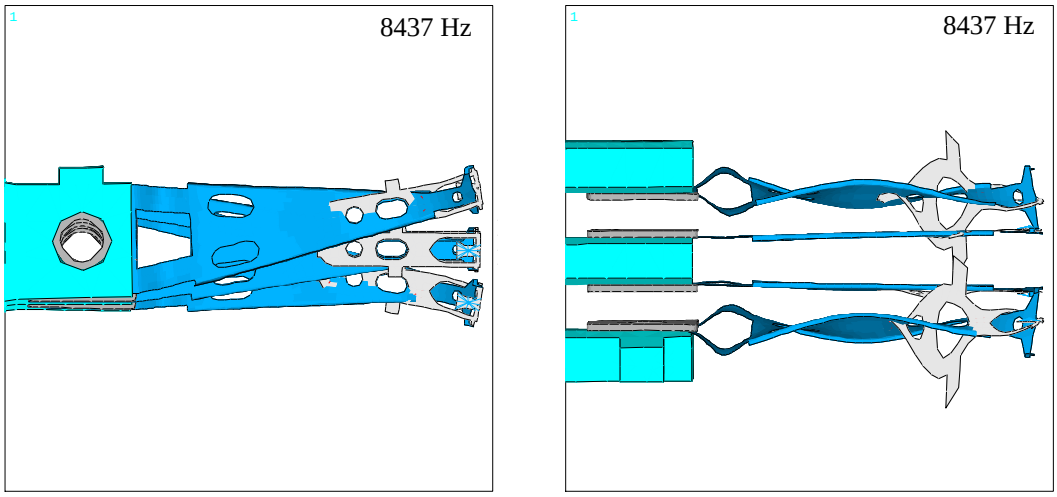

(a) Mode 37; isometric and top views

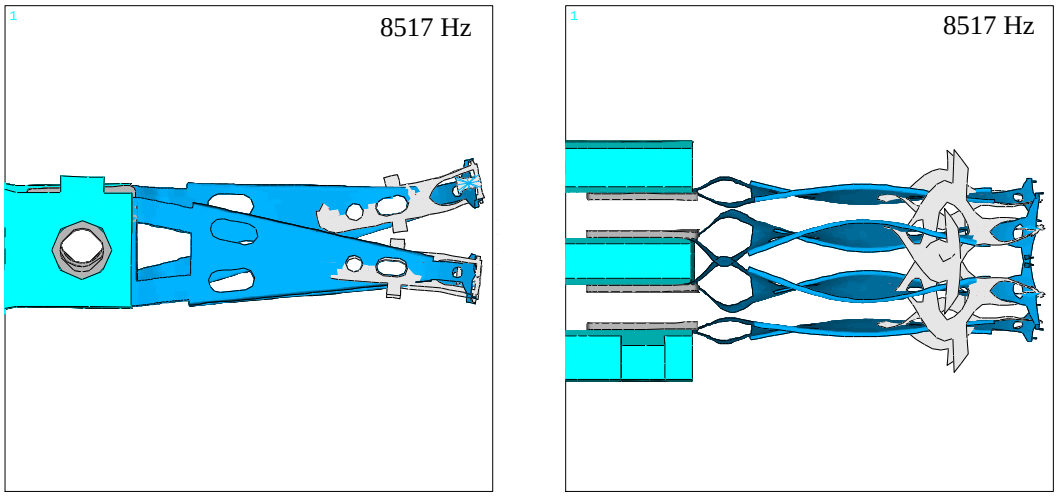

(b) Mode 38; isometric and top views

Figure 35: Two suspension sway modes

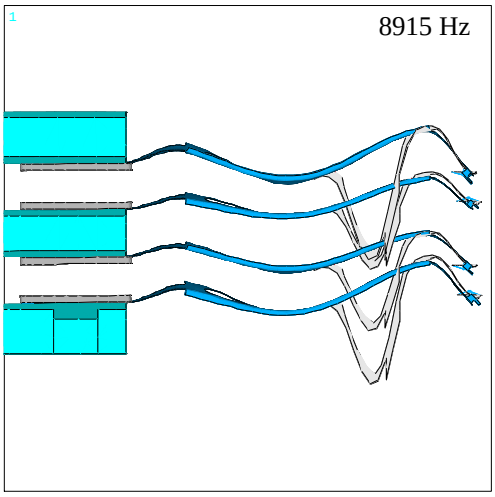

(a) Mode 40

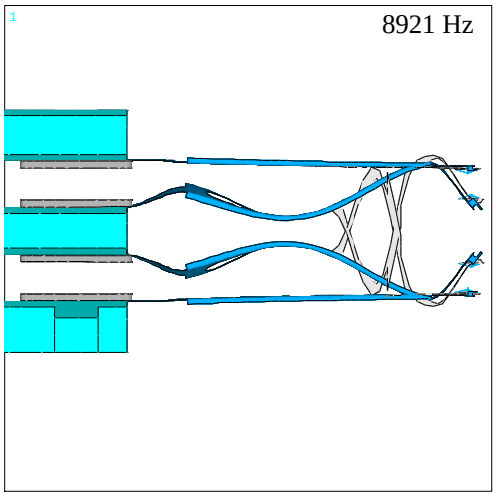

(b) Mode 41

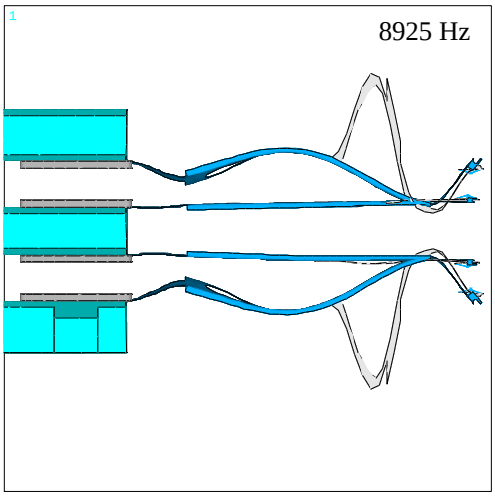

(c) Mode 42

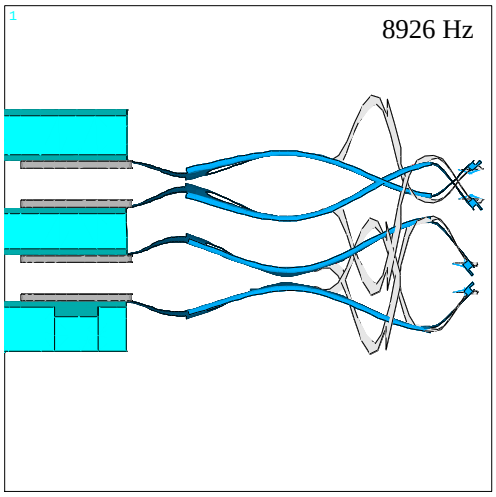

(d) Mode 43

Figure 36: Four suspension third bending modes

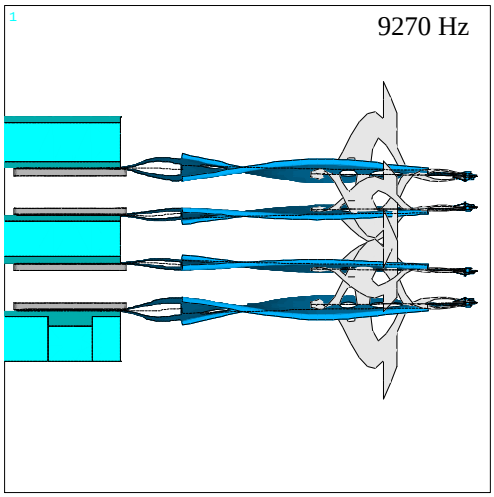

(a) Mode 46

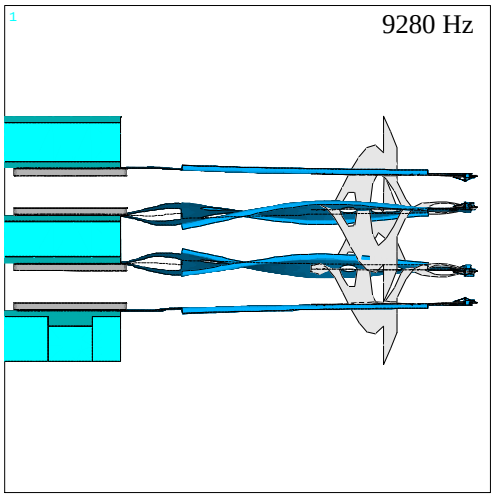

(b) Mode 47

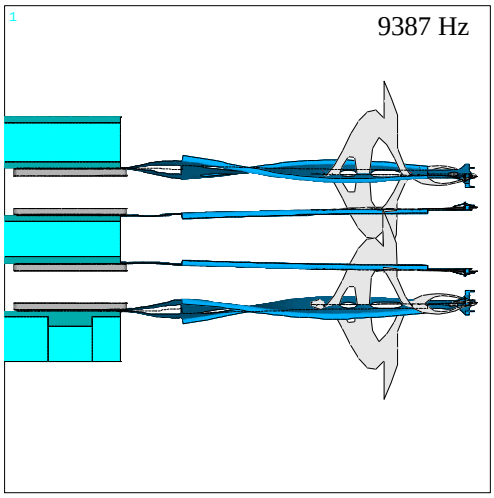

(c) Mode 48

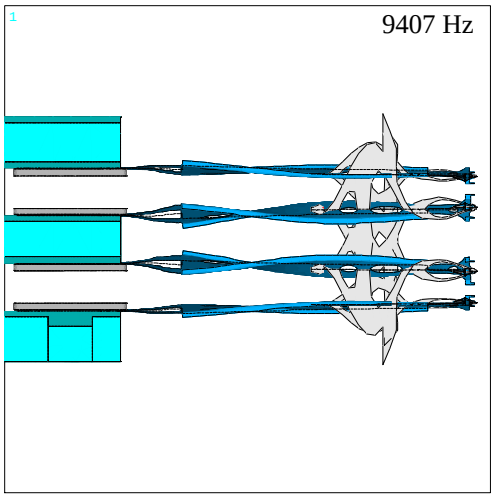

(d) Mode 49

Figure 37: Four flexure torsion/suspension second torsion modes

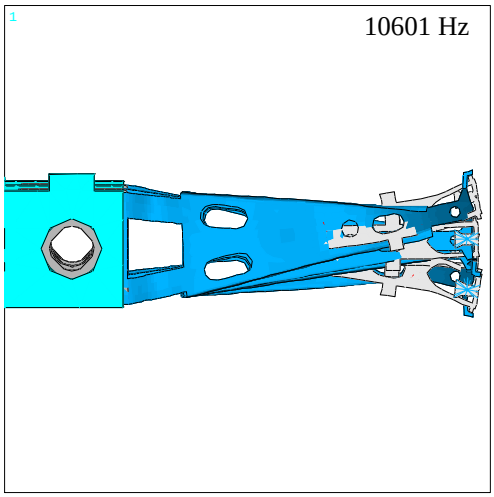

(a) Mode 56

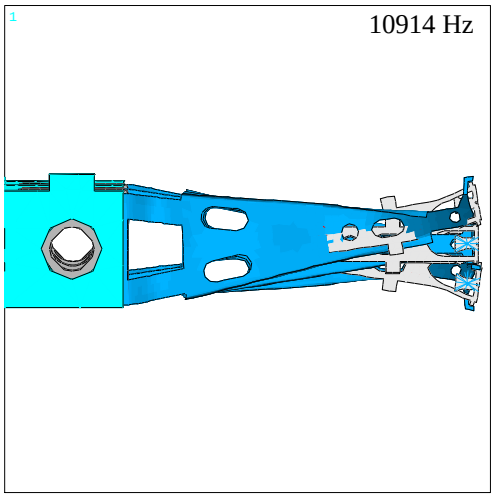

(b) Mode 57

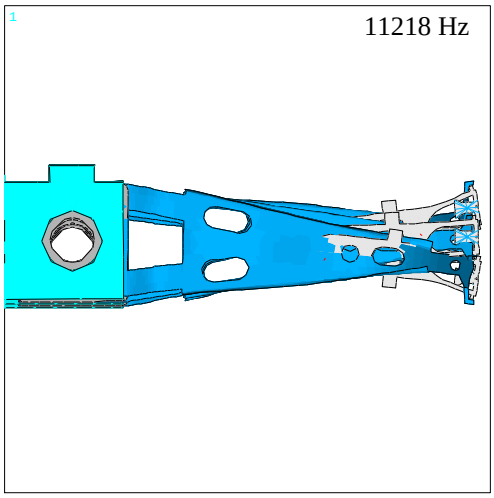

(c) Mode 58

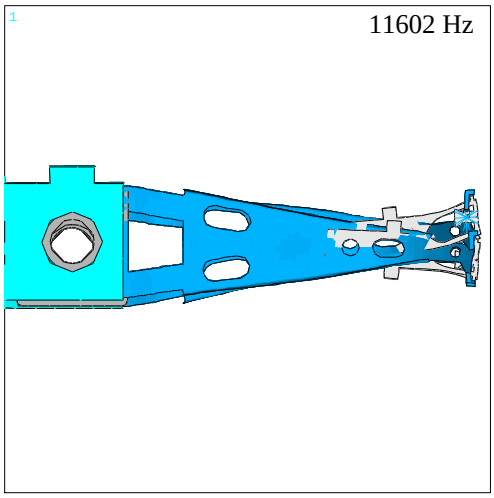

(d) Mode 60

Figure 38: Four suspension sway modes, lightly coupled with E-block torsion modes

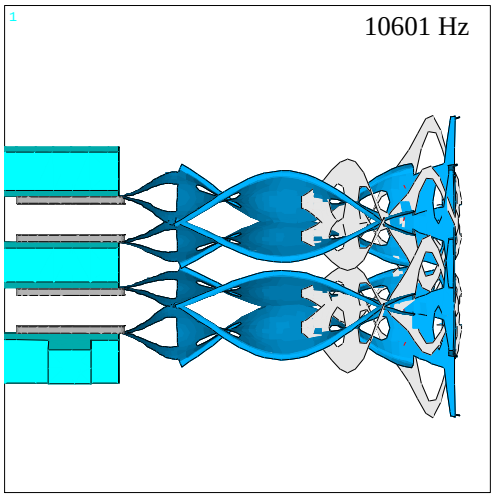

(a) Mode 56

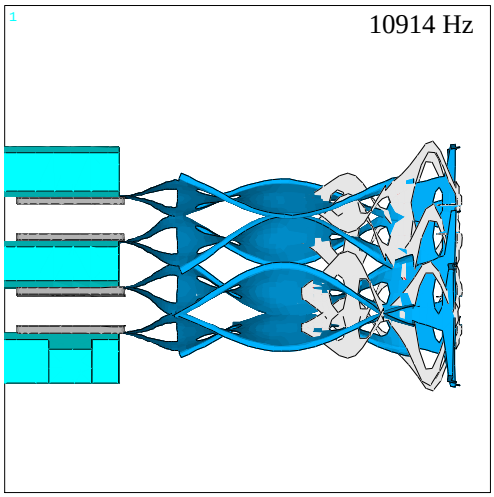

(b) Mode 57

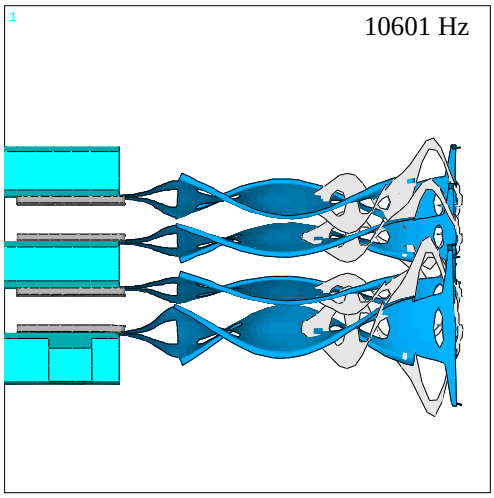

(a) Mode 56

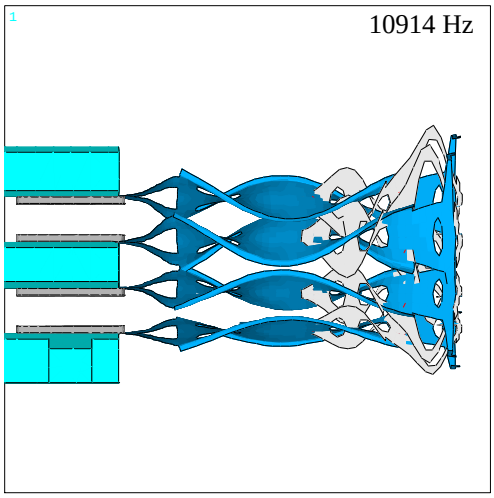

(b) Mode 57

Figure 39: Four suspension third torsion modes lightly coupled with E-block torsion modes

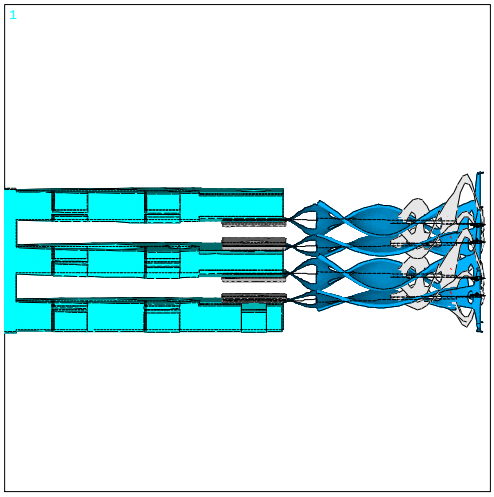

Figure 40: Suspension third torsion closely coupled with E-block first torsion mode

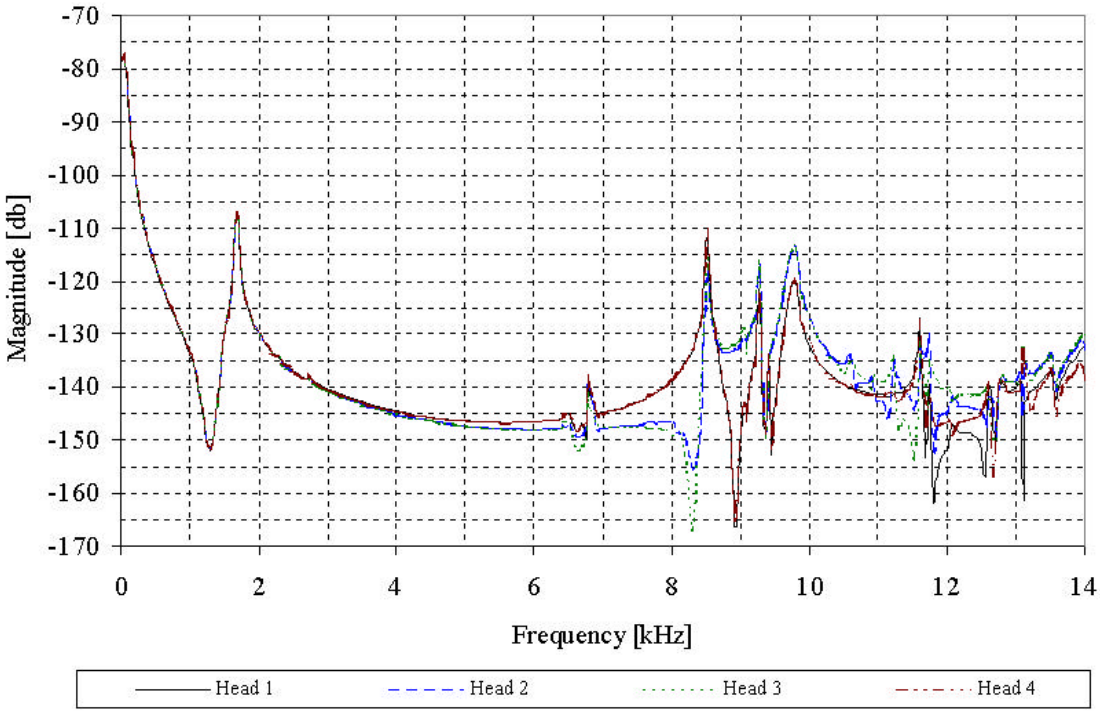

Figure 41: FRFs of the four sliders in the HSA: slider off-track response to a unit rotational excitation at the E-block pivot (about the pivot axis)